Optical and chemical properties and oxidative potential of aqueous-phase products from OH and ^{3}C*-initiated photooxidation of eugenol

Xudong Li[1], Ye Tao[1], Longwei Zhu[1], Shuaishuai Ma[1], Shipeng Luo[1], Zhuzi Zhao[1], Ning Sun[1], Xinlei Ge[2,*], Zhaolian Ye[1,*]

[1]College of Chemistry and Environmental Engineering, Jiangsu University of Technology, Changzhou 213001, China

[2]Jiangsu Key Laboratory of Atmospheric Environment Monitoring and Pollution Control, Collaborative Innovation Center of Atmospheric Environment and Equipment Technology, School of Environmental Sciences and Engineering, Nanjing University of Information Science and Technology, Nanjing 210044, China

*Correspondence: Zhaolian Ye (bess_ye@jsut.edu.cn) and Xinlei Ge (caxinra@163.com)

Abstract: Aqueous reactions may turn precursors into light-absorbing and toxic products, leading to air quality deterioration and adverse health effects. In this study, we investigated comprehensively eugenol photooxidation (a representative biomass burning emitted, highly substituted phenolic compound) in bulk aqueous phase with direct photolysis, hydroxyl radical (OH) and an organic triplet excited state (^{3}C*). Results show that the degradation rates of eugenol followed the order of ^{3}C*>OH >direct photolysis. During ^{3}C*-initiated oxidation, different reactive oxygen species (ROS) including ^{3}C*, OH, ^{1}O$_2$ and O$_2$$^{\bullet-}$ can participate in oxidation of eugenol, quenching experiments verified ^{3}C* was the most important one; while during OH-initiated oxidation, O$_2$$^{\bullet-}$ was a more important ROS than OH to ~~oxidize~~degrade eugenol. The rate constants under saturated O$_2$, air and N$_2$ followed the order of k_{O_2} > k_{Air} > k_{N_2}

26 for both direct photolysis and OH-initiated oxidation, but changed to $k_{Air} > k_{N_2} > k_{O_2}$

27 for $^3C^*$-mediated oxidation. pH and dissolved oxygen (DO) levels both decreased

28 during oxidation, indicating formation of acids and the participation of DO in oxidation.

29 UV-vis light absorption spectra of the reaction products showed clear absorbance

30 enhancement in the 300-400 nm range for all three sets of experiments and new

31 fluorescence at excitation/emission=250/(400-500) nm appeared, suggesting the

32 formation of new chromophores and fluorophores (brown carbon species); and these

33 species were likely attributed to humic-like substances (HULIS) as shown by the

34 increases of HULIS concentrations during oxidation. Large mass yields of products

35 (140%-197%) after 23 hours of illumination were obtained, and high oxidation degrees

36 of these products were also observed; correspondingly, a series of oxygenated

37 compounds were identified, and detailed reaction mechanism with functionalization as

38 a dominant pathway was proposed. At last, dithiothreitol (DTT) assay was applied to

39 assess oxidation potential of the reaction products, and the end products of all three sets

40 of experiments showed higher DDT consumption rates than that of eugenol, indicating

41 more toxic species were produced upon aqueous oxidation. Overall, our results by using

42 eugenol as a model compound, underscore the potential importance of aqueous

43 processing of biomass burning emissions in secondary organic aerosol (SOA)

44 formation.

45

1 Introduction

47   Photochemical reactions in atmospheric aqueous phases (cloud/fog droplets and

48 aerosol water) can affect lifetimes of many organic species, and are an important source

49 and pathway of secondary organic aerosol (SOA) formation (Vione et al., 2006; Zhao

et al., 2012). Compared to the ~~gasSOA~~SOA formed via gas-phase photochemical oxidation~~,~~ (gasSOA), aqueous-phase SOA (aqSOA) is often more oxidized and less volatile, therefore might play an important role in haze formation, air quality and global climate change (Ervens et al., 2011; Lim et al., 2010). However, due to complexity of the aqueous reactions and influencing factors (such as precursors, oxidants, and light intensities), detailed reaction mechanism, optical property, oxidative potential (OP) and the interplay among them remain poorly understood.

Many laboratory studies have focused on aqueous-phase oxidations of low molecular weight (LMW) volatile organic compounds (VOCs), such as isoprene, terpenes (α-, β-pinene), as well as their gas-phase oxidation products (such as glyoxal, methylglyoxal, *cis*-pinonic acid and methyl vinyl ketone) (Faust et al., 2017; Herrmann, 2003; Herrmann et al., 2015; Huang et al., 2011; Lee et al., 2012; Zhang et al., 2010). Recently, aqueous oxidation of semi-/intermediate volatility VOCs (S/IVOCs), such as the phenolic compounds emitted from combustion or pyrolysis of lignin in biomass, were also extensively investigated (Barzaghi and Herrmann, 2002; Bonin et al., 2007; Chen et al., 2020; Gilardoni et al., 2016; He et al., 2019; Jiang et al., 2021; Li et al., 2014; Li et al, 2021; Ma et al., 2021; Mabato et al., 2022; Smith et al., 2014; Sun et al., 2010; Tang et al., 2020; Yang et al., 2021; Yu et al., 2016; Lu et al., 2019). Generally, chemical structures of precursors have profound influences on the reaction mechanisms and products, while effect of oxidants also cannot be neglected. It is evident that liquid water can contain various types of oxidants, such as singlet oxygen ($^1O_2$), nitrate radical (NO_3), hydroxyl radical (OH), and organic triplet excited states ($^3C^*$), and all oxidants can play crucial roles in photooxidation reactions (Kaur and Anastasio, 2018; Scharko et al., 2014). Among them, OH is a ubiquitous oxidant with concentrations of 10^{-13}-10^{-12} mol·L^{-1} (Arakaki et al., 2013; Gligorovski et al., 2015; Herrmann et al., 2003). Hence,

aqueous OH-induced photooxidation has been extensively studied (Chen et al., 2020; Sun et al., 2010; Yu et al., 2016). Compared to OH oxidation, $^3C^*$-initiated aqueous oxidation (photosensitized reactions) has also attracted attentions in recent years (Ma et al., 2021; Wang et al., 2021). Several classes of organic compounds in ambient air, including non-phenolic aromatic carbonyls, quinones, aromatic ketones and nitrogen-containing heterocyclic compounds, can form $^3C^*$ after absorbing light (Alegría et al., 1999; Kaur et al., 2019; Nau and Scaiano, 1996; Rossignol et al., 2014; Chen et al., 2018). These compounds are termed photosensitizers. $^3C^*$ is capable of reacting with O_2 to produce singlet oxygen ($^1O_2$) and superoxide radicals ($O_2^{\bullet-}$). Various reactive oxygen species (ROS) can be generated and affect greatly the $^3C^*$-initiated aqueous-phase reactions. Despite some studies demonstrating importance of ROS in photochemical process (Ma et al, 2021; Wang et al., 2020; Wang et al., 2021), our current understanding on $^3C^*$-initiated oxidation is still limited.

Excitation-emission matrix (EEM) fluorescence spectroscopy, as a low-cost, rapid, non-destructive and high-sensitivity technique, can offer detailed information on chromophores hence has been widely employed for studies of aquatic dissolved organic matter (Aryal et al., 2015). Nevertheless, it has not been extensively used in atmospheric aerosol research (Mladenov et al., 2011). Prior studies have investigated the relationship between the fluorescence components and chemical structures of atmospheric aerosols by using high-resolution aerosol mass spectrometry (AMS) and EEM fluorescence spectroscopy (Chen et al., 2016a; Chen et al., 2016b). An earlier report from Chang and Thompson (2010) found fluorescence spectra of aqueous-phase reaction products of phenolic compounds, which had some similarities with those of humic-like substances (HULIS), and Tang et al. (2020) reported that aqueous photooxidation of vanillic acid could be a potential source of HULIS. Chang and

4

Thompson (2010) also showed that light-absorbing and fluorescent substances generally had large conjugated moieties (i.e., quinones, HULIS, polycyclic aromatic hydrocarbons (PAHs)), which can damage human body (Dou et al., 2015; McWhinney et al., 2013). HULIS are considered as an important contributor to induce oxidative stress since they can serve as electron carriers to catalyze ROS formation (Dou et al., 2015; Ma et al., 2019; Huo et al., 2021; Xu et al., 2020), causing adverse health effects. Dithiothreitol (DTT) assay (Alam et al., 2013; Verma et al., 2015), as a non-cellular method, was widely employed to determine oxidation activity and OP of atmospheric PM (Chen et al., 2019; Cho et al., 2005) for the evaluation of its health effects. Some other works (Fang et al., 2016; McWhinney et al., 2013; Verma et al., 2015; Zhang et al., 2022) focused on the link between chemical components and OP in PM, and confirmed that several kinds of compounds, such as quinones, HULIS and transition metals usually had strong DTT activities. However, DTT method is rarely used to evaluate the OP of aqueous-phase oxidation products previously (Ou et al., 2021).

In the present work, we chose eugenol (ally guaiacol) as a model compound to conduct aqueous oxidation experiment. As a representative methoxyphenol emitted from biomass burning (BB) (Hawthorne et al., 1989; Simpson et al., 2005), it was widely detected in atmospheric particles. For instance, concentration and emission factor of this compound from beech wood burning were 0.032 $\mu g/m^3$ and 1.534 $\mu g/g$, which were twice those of guaiacol (0.016 $\mu g/m^3$ and 0.762 $\mu g/g$) (Bari et al., 2009). Eugenol is a semivolatile aromatic compound with a moderate water-solubility (2.46 g/L at 298 K). Chemical characteristics of aqueous reaction products under direct photolysis (without oxidant) and oxidations by OH radicals and $^3C^*$ triplet states, were comprehensively elucidated by a suite of analytical techniques including high-performance liquid chromatography (HPLC), ultraviolet and visible (UV-Vis)

spectrophotometry, gas chromatography mass spectrometry (GC-MS), and soot particle

aerosol mass spectrometry (SP-AMS). Moreover, light absorption, fluorescent and

oxidative properties of the aqueous oxidation products were also investigated.

2 Materials and methods

2.1 Chemicals and reagents

Eugenol (99%), tert-butanol (TBA, 99%), 3,4-dimethoxybenzaldehyde (DMB, 99%), para-benzoquinone (p-BQ, 99%), dithiothreitol (99%) and 5,5′-dithiobis-2-nitrobenzoic acid (DTNB, 99%), 2-nitro-5-thiobenzoic (99%), 5,5-dimethyl-1-pyrroline N-oxide (DMPO)**,** 2,2,6,6-tetramethylpiperidine (TEMP) were all purchased from Sigma-Aldrich. Superoxide dismutase (SOD) was purchased from Bovine Erythrocytes BioChemika. Dichloromethane (HPLC-MS grade, 99%), methanol (HPLC-MS grade, 99%), acetonitrile (HPLC-MS grade, 98%), hydrogen peroxide (H_2O_2, 35 wt %), and 2,4,6-trimethylphenol (TMP, 99%) were all obtained from Acros Chemicals. Sodium azide (NaN_3, 98%) was purchased from J&K Scientific Ltd. (Beijing, China). All solutions were prepared using ultrapure water (Millipore) on the days of experiments.

2.2 Photochemical oxidation experiments

Aqueous-phase photochemical reactions were carried out in a Rayonet photoreactor (model RPR-200) equipped with 16 light tubes (2 RPR-3000, 7 RPR-3500 and 7 RPR-4190 tubes), which was frequently used to mimic sunlight for photochemical experiments and was described in details by several groups (George et al., 2015; Hong et al., 2015; Huang et al., 2018; Jiang et al., 2021; Zhao et al., 2014).

147 Pyrex tubes containing sample solutions were placed in the center and received

148 radiation from surrounded lamps of all sides. To ensure mixing of the solution, a fan

149 and a magnetic stir bar were placed at the bottom of the reaction tube. The solution

150 temperature was controlled at 25 ± 2°C. The same photoreactor system and a normalized

151 distribution of photon fluxes inside the reactor have been reported elsewhere (George

152 et al., 2015), and the wavelength of light was in the range of 280~500 nm. We only

153 measured light intensity at the surface of the solution with a radiometer (Photoelectric

154 instrument factory of Everfine Corporation, Hangzhou, China), which was determined

155 to be ~2400 μW/cm^2 in the range of 290-320 nm (UVB), lower than the sunlight

156 intensity (6257.1 μW/cm^2).

157   In this work, 300 μM H_2O_2 and 15 μM DMB were added into solutions as sources

158 of OH and $^3C^*$, respectively. The initial concentration of eugenol was 300 μM. For $^3C^*$-

159 mediated experiments, solutions were adjusted to pH=3 by sulfuric acid in order to

160 perform experiments under optimal conditions (Ma et al., 2021; Smith et al., 2014)

161 since DMB triplet state is protonated to a more reactive form in acidic solution. We

162 conducted three sets of oxidation experiments: (A) 300 μM eugenol + 300 μM H_2O_2,

163 (B) 300 μM eugenol + 15 μM DMB, and (C) 300 μM eugenol without oxidants. In each

164 series of experiments, a dark control experiment was performed synchronously with a

165 Pyrex tube wrapped by aluminum foil. Results showed loss of eugenol under dark

166 conditions were negligible (data not shown). In addition, to evaluate the roles of ROS

167 in eugenol degradation during $^3C^*$-initiated oxidation, quenching experiments by using

168 specific scavengers to capture different ROS were performed, namely TBA for OH,

169 NaN_3 for $^1O_2$, SOD for $O_2^{\cdot-}$, and TMP for $^3C^*$, respectively (Pan et al., 2020; Chen et

170 al., 2020). For OH-initiated oxidation, quenching experiments using p-BQ for $O_2^{\cdot-}$ (Ma

171 et al., 2019; Raja et al., 2005), and TBA for OH were conducted. For most experiments,

7

172   solutions were saturated by air and each experiment presented was repeated three times

173   unless otherwise stated. Average results with one standard deviation were provided. In

174   order to further evaluate the role of oxygen in photooxidation, experiments were also

175   conducted by using different saturated gases (air, N_2 and O_2).

2.3 Analytical methods

176

2.3.1 Determination of eugenol concentrations

177

178   Before and during the photochemical experiment, 2 mL of reacted solution was

179   sampled periodically and subjected to HPLC (LC-10AT, Shimadzu, Japan) analysis to

180   quantify eugenol concentration. The HPLC was equipped with an InertSustain AQ-C18

181   reverse phase column (4.6×250 mm, 5.0 μm, Shimadzu) and a UV-vis detector. The

182   mobile phase was a mixture of acetonitrile/H_2O (v/v: 60/40) at a flow rate of 0.6

183   mL/min, and the detection wavelength was 280 nm. The first-order kinetic rate constant

184   of eugenol degradation can be obtained from the slope of plot of $-\ln(c_t/c_0)$ versus

185   reaction time, as presented in Eq.(1).

186                         $$\ln(c_t/c_0)=-kt \qquad\qquad (1)$$

187   Where c_0 and c_t are eugenol concentrations (in μM) at the initial and reaction time

188   t, while k represents the pseudo first-order rate constant (in s^{-1}).

2.3.2 UV-vis and fluorescent spectra

189

190   The UV-vis light ~~absorbance~~absorption spectra of reacted solutions (placed in a 1

191   cm path length quartz cuvette) were measured by using an UV-vis spectrophotometer

192   (Specord 210 plus, Analytik Jena., Germany). The instrument has a dual-beam optical

193   system with tungsten and deuterium lamps as light sources. A reference absorption

8

194 spectrum of ultrapure water was carried out in the same cuvette prior to sample analysis

195 for baseline correction.

196   Immediately after the UV-Vis measurement, the cuvette was transferred to a three-

197 dimensional EEM fluorescence spectrometer (FluoroMax Plus，HORIBA Scientific).

198 The ranges of wavelength varied from 200 to 450 nm for excitation wavelengths (Ex)

199 and from 290 to 650 nm for emission wavelength (Em). Intervals of the excitation and

200 emission wavelengths were 5 nm and 2 nm, respectively. The reported absorbance and

201 EEM spectra here are averages of the results from experiments in triplicate.

202 **2.3.3 Determination of HULIS concentrations**

203   Solid phase extraction (SPE) cartridges (CNW Poly-Sery HLB, 60 mg/cartridge)

204 were used to isolate HULIS from the reaction products. The SPE cartridge was first

205 rinsed with 1 mL ultrapure water and 3 mL methanol prior to extraction. The solution

206 was acidified to pH ~2 using HCl and loaded on an SPE cartridge, which was rinsed

207 with 1 mL ultrapure water again. Next, 3 mL methanol/ammonia (98:2, v/v) mixture

208 was added into the SPE cartridge to elute HULIS, and the solution was blown to full

209 dryness with high purity N_2, followed by dilution with ultrapure water to 25 mL for

210 quantification of HULIS using the HPLC coupled with an evaporative light scattering

211 detector (ELSD3000). Recovery efficiency of the HULIS standard, Suwanne River

212 Fulvic Acid (SRFA), was 75-80% with the standard deviation of reproducibility less

213 than 5%. More details have been described elsewhere (Tao et al., 2021).

214 **2.3.4 Oxidative potential (OP) based on DTT assay**

215   The OP of reaction products was determined by the DTT method (Cho et al., 2005;

216 Lin and Yu, 2019) with slight improvements. Briefly, 1.2 mL sample solution was

transferred into a 10 mL glass tube, then 6 mL phosphate buffer (0.1 M, pH 7.4) and 300 µL of 2.5 mM DTT were added and mixed thoroughly. The DTT mixed solution was placed in a 37℃ water bath for incubation. Over the course of reactions that lasted for 150 minutes, 1 mL aliquot of DTT mixture was taken every 30 minutes, and 100 µL of 5 mM DTNB (prepared in 0.1 mM phosphate buffer) was added and loaded in a centrifuge tube. Next, reactions between DTNB and DTT produced bright yellow TNB, which was quantified by the UV-Vis spectrometer within 30 minutes. Finally, we measured the light absorbance (A_t) at 412 nm to indirectly quantify the remaining DTT. Another 1.2 mL ultrapure water instead of sample solution was treated in the same way and the absorbance was denoted as A as the blank value. A_0 represents the initial light absorbance value. Thus, DTT concentration consumed by the sample solution (M_{DTT}, µM) and that by the blank solution (M_{DTT0}, µM) can be calculated according to Eq.(2) and Eq.(3), respectively.

$$M_{DTT} = \frac{A_0 - A_t}{A_0} \times C_{DTT_0} \tag{2}$$

$$M_{DTT0} = \frac{A_0 - A}{A_0} \times C_{DTT_0} \tag{3}$$

Here, C_{DTT0} was the initial DTT concentration in sample solution (100 µM in this work). DTT consumption rates (R_{DTT} and R_{DTT0}) were then obtained from the slopes of plots of M_{DTT} and M_{DTT0} versus incubation times. Experiments of blanks and samples were typically run in a triplicate. The reproducibility of the whole analysis showed that the relative standard deviation of DTT consumption rate was 3-4%.

2.3.5 Product analysis by GC-MS

Reacted solution (about 30 mL) was extracted with 10 mL dichloromethane twice. The extract was concentrated into 1 mL by blowing N_2 gently, subsequently transferred to a 2 mL vial, and analyzed by a GC-MS (7890A GC/5975C MS, Agilent) with a DB-

241 5ms capillary column (30 m×0.25 mm×0.5 μm). The operational conditions were set as

242 follows: injector was at 200℃; ion source was at 230 ℃; column oven temperature was

243 programmed to be held at 35℃ for 4 minutes, then ramped to 250 ℃ at a rate of

244 20℃/minute and held for 10 minutes. The recovery efficiency, method detection limits

245 and quality assurance/quality control have been described in our previous work (Ye et

246 al., 2020).

2.3.6 SP-AMS analysis and mass yields of reaction products

248 An Aerodyne SP-AMS (Onasch et al., 2012) was applied to analyze the low-

249 volatility organic products, similar to our previous work (Chen et al., 2020; Ge et al.,

250 2017). SP-AMS data were acquired in V mode and analyzed by Squirrel v.1.56D and

251 Pika v1.15D software. The organic fragments were classified into six groups: CH, CHO,

252 CHN, CHO_2, CHON and HO. Elemental ratios (oxygen-to-carbon, O/C; hydrogen-

253 to-carbon, H/C), were calculated according to the method proposed by Canagaratna et

254 al. (2015).

255 Since the AMS analysis requires nebulization of sample solution into particles

256 before determination, and quantification of organics was influenced by the atomization

257 efficiency and carrier gas flow, we thus cannot use SP-AMS measured concentration to

258 quantify the mass of products directly. In this case, according to Li et al. (2014), we

259 added an internal standard (SO_4^{2-}) prior to AMS analysis, and the mass ratio of particle-

260 phase organics to SO_4^{2-} ($\Delta Org/SO_4^{2-}$) can be used to calculate the mass concentration

261 of products. Furthermore, the mass yield of aqueous-oxidation products ($Y_{products}$, %),

262 which is the mass of products generated per unit mass of precursor consumed, can be

263 calculated according to Eq. (4).

264
$$Y_{products}(\%) = \frac{(\Delta Org/SO_4^{2-})[SO_4^{2-}]_0}{C_0 M \eta} \times 100\% \tag{4}$$

265 Where $[SO_4^{2-}]_0$ is the SO_4^{2-} concentration (here 7.27 mg/L), C_0 is the initial eugenol

266 concentration (in mmol/L), M is MW of the precursor (164 g/mol for eugenol) , and η

267 is the degraded fraction of eugenol.

3 Results and discussion

3.1 Kinetics of aqueous photooxidation

270 Figure 1 shows unreacted eugenol concentrations (c_t) and the negative logarithm

271 of c_t/c_0 (-ln(c_t/c_0)) as a function of reaction time, respectively. The pseudo first-order

272 rate constants (k) obtained by Eq.(1) were also presented. As described in Fig. 1a,

273 eugenol concentration decreased to be <20% of the initial concentration in 3 hours,

274 suggesting photooxidation was fast under all three reaction conditions. In the presence

275 of $^3C^*$, eugenol was degraded nearly 100% after 3 hours. Previous study (Chen et al.,

276 2020) on $^3C^*$-initiated 4-ethylguaiacol oxidation reports a time of 21 hours for a

277 complete degradation. Apart from difference of precursors, different light irradiation

278 spectra and stronger energy of light in this work than the previous work might be

279 responsible for the fast loss of eugenol. The bond dissociation energies (BDEs) are 340

280 kJ/mol for OH, 374 kJ/mol for C-H in $-CH_3$ group, 345 kJ/mol for C=C bond, and 403

281 kJ/mol for C-H in $-OCH_3$ group, respectively (Herrmann et al., 2003; He et al., 2019).

282 Due to influences of steric hindrance and intramolecular hydrogen bonding, the H-

283 abstraction from OH group might not be favorable and the most probable H-abstraction

284 might take place in C=C of the allyl group. As a result, breakage of C=C into C-C at

285 the allyl group can lead to the formation of 2-methoxy-4-propyl-phenol (Section 3.6.1).

286 When photon energy is higher than the BDE, chemical bonds can break, leading to

287 decomposition of compounds and possibly further mineralization. The energy of photon

288 of 300 nm is 412 kJ/mol and can break all major bonds in eugenol, while the energy of

289 350 nm is 353 kJ/mol, being able to break some of the bonds in eugenol as well. Overall,

290 eugenol can be easily decomposed after absorbing the photons.

291 As shown in Fig. 1b, the first-order rate constants were 2.43×10^{-4} s^{-1}, 2.73×10^{-4} s^{-1}

292 ^{1}, and 5.75×10^{-4} s^{-1} for direct photolysis and photooxidations by OH and $^3C^*$,

293 respectively. $^3C^*$-initiated photooxidation was quicker than that attacked by OH, likely

294 due to combined contributions from reactions with $^1O_2$, $O_2^{\cdot-}$ and OH (Section 3.2).

295 Similar results were found for aqueous phase reactions of three phenols against OH and

296 $^3C^*$ by Yu et al. (2016) (Note the initial concentrations of H_2O_2 and DMB were 100 µM

297 and 5 µM, respectively, with the same ratio as 300 µM H_2O_2 to 15 µM DMB in this
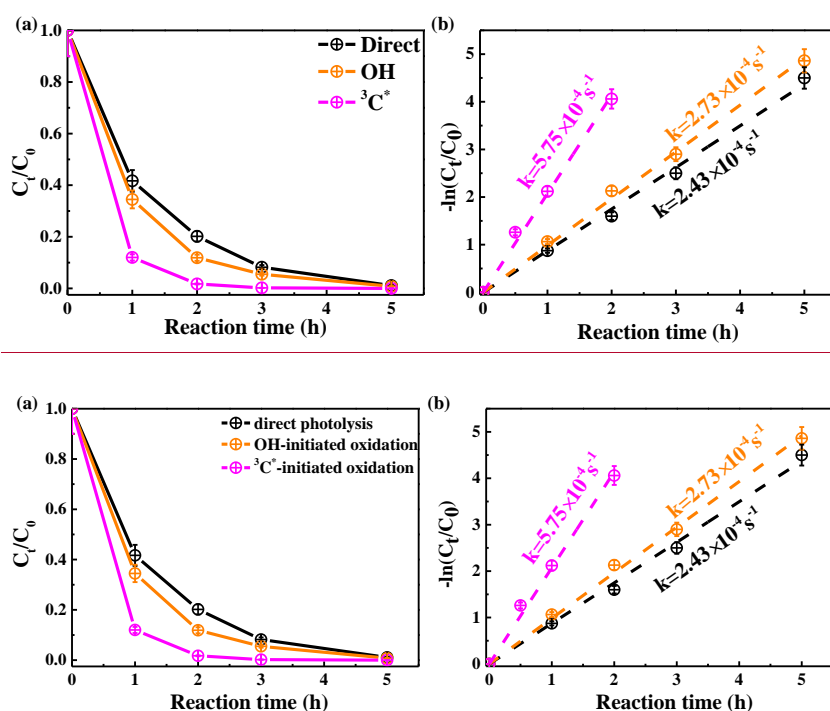
298 work)

301 **Figure 1.** Aqueous-phase eugenol decay kinetic curves (a) and first-order rate constants (b) obtained

302 based on Equation 1 under direct photolysis, OH-initiated oxidation and $^3C^*$-initiated oxidation.

303 Error bar represents one standard deviation from the measurements in triplicate.

3.2 Relative importance of ROS in photooxidation

3.2.1 Quenching experiments in $^3C^*$-initiated photooxidation

306   Relative importance of different ROS in photooxidation can be investigated by

307 addition of scavengers/quenchers, and then be evaluated based on the different

308 degradation efficiencies of eugenol in absence and presence of the corresponding ROS

309 quenchers. For each quencher, we conducted several gradient experiments with varying

310 molar ratios of eugenol to quencher. The ratios were 0.075:1, 0.15:1, 0.3:1, 0.75:1, 1.5:1

311 for quenchers of NaN$_3$, TMP and TBA, and 1.2:1, 1.6:1, 2.5:1, 5:1, 10:1 for SOD, which

312 were all within the typical ranges of ROS quenching experiments reported previously

313 (Zhou et al., 2018). Excess concentrations of quenchers have been added repeatedly to

314 ensure the complete reactions between ROS and scavengers. Figure 2 displays the

315 impacts of quenchers on eugenol degradation. All rate constants (k) with quenchers

316 were lower than those of the quencher-free solutions. The optimum molar ratio of

317 eugenol to quencher was selected such that the eugenol degradation did not change with

318 the increase of added quencher (Wang et al., 2021). For example, along with the

319 decrease of molar ratios of eugenol to NaN$_3$ from 1.5:1 to 0.075:1, the variation of

320 eugenol degradation was stabilized at the ratio of 0.15:1, indicating that $^1O_2$ has been

321 completely quenched at this ratio, therefore a molar ratio of 0.15:1 for NaN$_3$ was

322 optimal, since excess scavenger may generate other products that interfere the existing

323 reactions. Finally, the optimal molar ratios of eugenol to quenchers of TBA, NaN$_3$, TMP

324 and SOD, were determined to be 1.5, 0.15, 0.075 and 2.5, respectively. Table 1 and Fig.

325 S1 compared the rate constants determined under the ratios above and they were in an

14

326 order of TMP<NaN$_3$<SOD<TBA, suggesting relative importance of generated ROS to

327 eugenol degradation was in the order of $^3C^*$＞$^1O_2$＞$O_2^{\bullet-}$＞OH. This result suggests that

328 $^3C^*$ plays a major role among all ROS in the photooxidation. Previously, Laurentiis et

329 al. (2013) reported that 4-carboxybenzophenone (70 μM) could act as $^3C^*$ and the

330 photosensitized degradation was more effective than oxidants such as OH, O$_3$;

331 Misovich et al. (2021) investigated the aqueous DMB-photosensitized reaction (5 μM,

332 same as in this study) also demonstrated that $^3C^*$ was the greatest contributor to phenol

333 or guaiacyl acetone degradation, followed by $^1O_2$, while both OH and $^1O_2$ contributions

334 were relatively minor.

335 To further assess the relative importance of different ROS, we propose to use the

336 following Eq.(5) for a rough estimation:

337 $$Red_{ROS} \text{ (in \%)= } (k-k_{quencher})/k*100\% \tag{5}$$

338 Here k (in s^{-1}) is the original rate constant of $^3C^*$-initiated oxidation (or OH-initiated

339 oxidation in Section 3.2.2) and $k_{quencher}$ (in s^{-1}) is the rate constant after the target ROS

340 has been completely scavenged by its quencher. k and $k_{quencher}$ in fact refer to those

341 reported in Fig. S1b. Red_{ROS} then refers to the percentages of reduction due to addition

342 of quencher for a ROS.

343 According to Eq.(5), Red_{3C^*} was calculated to be 85.7%. Similarly, the values of

344 $^1O_2$, $O_2^{\bullet-}$ and OH were 80.5%, 61.4% and 53.9%, respectively. Note Red_{ROS} only

345 reflects the relative important of ROS and it does not corresponds to the exact

346 contribution of that ROS in eugenol degradation without quenchers. The reason is that

347 although the addition of a ROS scavenger can eliminate oxidation by this ROS, but it

348 also significantly interrupts the original chain reactions as compared to those in the

349 absence of the scavenger, and reactions with other ROS might be enhanced. In this

350 regard, the sum of the four Red_{ROS} values may exceed 100%. Therefore, one should be

351   cautious to use Red$_{ROS}$ as a precise quantification of the ROS contribution in aqueous

352   oxidation. Determination of ROS concentrations during oxidation should be instead be

353   an effective way to elucidate the role of ROS. Here, we tried to detect in-situ generated

354   OH, $O_2^{\bullet-}$ and $^1O_2$ during photochemical reactions using a micro electron spin resonance

355   (ESR) spectrometer (Bruker Magnettech, Berlin, Germany) with DMPO as the spin trap

356   to form stable DMPO-OH or DMPO-$O_2^{\bullet-}$, with TEMP to capture $^1O_2$ to produce TEMP-

357     $^1O_2$ spin-adduct (TEMPO). The radicals can be identified and quantified by the peak

358   patterns in ESR spectra, such as the quarter line with a height ratio of 1:2:2:1 for

359   DMPO-OH, 1:1:1:1 for DMPO-$O_2^{\bullet-}$ and 1:1:1 for TEMP-$^1O_2$ (Guo et al., 2021).

360   Unfortunately, OH radical cannot be detected since its concentration might be lower

361   than the detection limit of the instrument (Fig. S2, ESR spectra of OH). In contrast, we

362   were able to detect high concentrations of $^3C^*$ and found the intensity of TEMP-$^1O_2$

363   signal reached its maximum at 30 minutes, then decreased slowly (Fig. S2, ESR spectra

364   of $^1O_2$). Combining the great quenching effect of TMP with high $^1O_2$ concentration from

365   ESR method, we can conclude that $^3C^*$ and $^1O_2$ play relatively important roles in
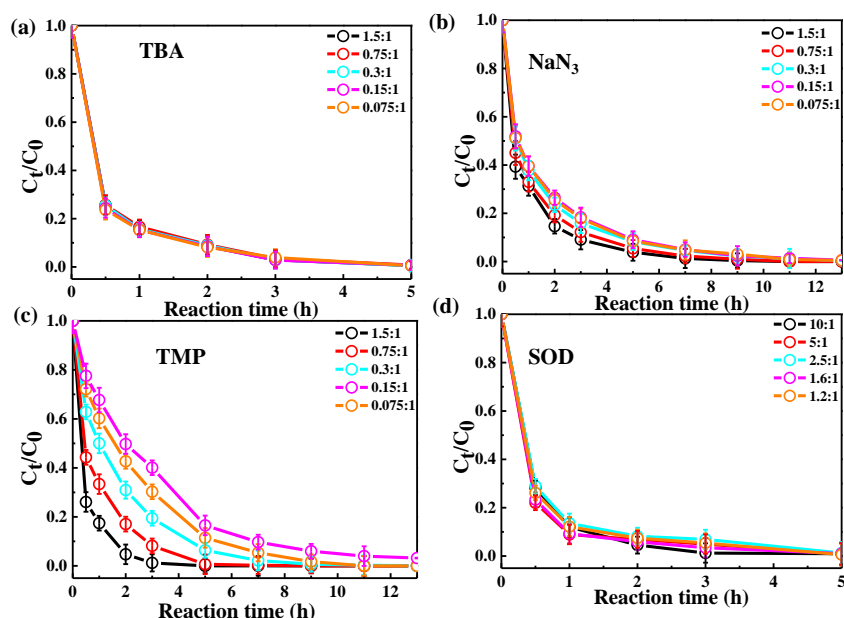
366   eugenol photooxidation.

Figure 2. Ratio of unreacted eugenol concentration to its initial concentration (C_t/C_0) at different molar ratios of eugenol to quencher, as a function of reaction time: (a) TBA, (b) NaN$_3$, (c) TMP and (d) SOD.

3.2.2 Quenching experiments in OH-initiated photooxidation

To examine the contributions of ROS to eugenol degradation for OH-initiated oxidation, TBA and p-BQ as trapping agents were added. Similar to ^{3}C*-initiated oxidation, several gradient experiments with varying molar ratios of eugenol to quenchers were conducted. The ratios were set as 6.5:1, 3.2:1, 1.6:1, 1.1:1 and 0.8:1 for p-BQ and 3.0:1, 1.5:1, 0.75:1, 0.3:1 and 0.15:1 for TBA. According to Fig. S3, molar ratio only had a slight influence on eugenol degradation, although degradation can be inhibited effectively by quenchers. Thus, we determined the appropriate molar ratios of 0.8 and 0.75 for p-BQ and TBA, respectively, as excess scavengers might influence the

381 chemical reactions.

382   Variations of the rate constants for the aforementioned quenching experiments were

383 determined, in comparison with those conducted without quenchers, and results are

384 listed in Table 1 and presented in Fig. S4. For TBA quenching tests, the rate constant

385 decreased by 18.7% (from 2.73×10^{-4} s^{-1} to 2.22×10^{-4} s^{-1}), showing that OH radical

386 played a certain role in eugenol photooxidation. Since H_2O_2 was mainly photolyzed at

387 wavelength <300 nm to generate OH radical, irradiation above 300 nm did not affect

388 the reaction significantly. The *p*-BQ could quench $O_2^{\bullet-}$, further suppressing the

389 generation of other ROS (e.g., •HO_2), therefore the rate constant decreased the most

390 (from 2.73×10^{-4} s^{-1} to 1.20×10^{-4} s^{-1}), suggesting $O_2^{\bullet-}$ was important for eugenol

391 photooxidation. This hypothesis could be further confirmed by the decline of rate

392 constant under N_2-saturated solution (Section 3.2.3). However, it was difficult to detect

393 both OH and $O_2^{\bullet-}$ directly due to their relatively short lifetimes and low concentrations

394 via ESR in this work.

395

396   **Table 1.** The first-order rate constants of eugenol in the presence of various scavengers. The initial

397   conditions were as follows: 300 μM eugenol; molar ratios of eugenol to quenchers TBA, NaN$_3$,

398   TMP and SOD, of 1.5, 0.15, 0.075 and 2.5, respectively; molar ratios of eugenol to quenchers p-BQ

399   and TBA of 0.8 and 0.75, respectively.
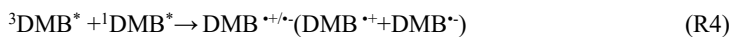
$^3C^*$-initiated quenching experiments			
Quenchers	ROS	Reaction rate constant k (s^{-1})	Pearson's R^2
no quencher	-	5.75×10^{-4}	0.996
TBA	OH	2.65×10^{-4}	0.999
SOD	$O_2^{\cdot-}$	2.22×10^{-4}	0.995
NaN$_3$	$^1O_2$	1.12×10^{-4}	0.999
TMP	$^3C^*$	0.82×10^{-4}	0.999
OH-initiated quenching experiments			
Quenchers	ROS	Reaction rate constant k (s^{-1})	R^2
No quencher	-	2.73×10^{-4}	0.995
TBA	OH	2.22×10^{-4}	0.998
p-BQ	$O_2^{\cdot-}$	1.20×10^{-4}	0.995

400

401   3.2.3 Influences of different saturated gases

402   In order to assess the role of O$_2$ in eugenol degradation, a series of experiments

403   were performed under both O$_2$-saturated and N$_2$-saturated conditions in addition to air.

404   N$_2$ gas was purged into reaction solution for ~30 minutes before experiment to achieve

405   the O$_2$-free condition. Figure 3 compared the changes of eugenol concentrations and

406   rate constants under the three gas conditions for direct photolysis, OH-initiated and $^3C^*$-

407   initiated oxidations, respectively. The rate constants followed the order of $k_{O_2} > k_{Air} >$

408   k_{N_2} under both direct photolysis and OH oxidation, providing evidence in support of O$_2$

409   being significant for eugenol degradation. This might be explained by the fact that O$_2$

410   can act as an electron acceptor to generate $O_2^{\cdot-}$ and $\cdot HO_2$, and subsequently form H$_2$O$_2$

411   and OH. For direct photolysis, rate constant under O$_2$-saturated condition increased

412   14.4% while it decreased 19.3% under N$_2$ saturation from that under saturated air. For

413 OH-initiated oxidation, the difference of rate constants under three saturated gases

414 became more distinct.

415   On the contrary, rate constants followed the order of $k_{Air} > k_{N_2} > k_{O_2}$ in $^3C^*$-

416 initiated oxidation. There are two possible explanations. On one hand, under N_2-

417 saturated condition without oxygen, DMB would involve in reactions (R1-R4), leading

418 to a more effective generation of $^3DMB^*$ therefore a higher degradation efficiency than

419 under O_2-saturated condition. On the other hand, for air/O_2-saturated solutions,

420 irradiation of DMB and eugenol would involve also reactions (R5-R8) in addition to

421 (R1-R4), and as a result, the amount of $^3DMB^*$ decreased, due to formation of other

422 ROS ($^1O_2$, $O_2^{\bullet-}$, OH, etc) with relatively weak oxidative capacities. In summary,

423 quenching of $^3DMB^*$ by ground state molecular oxygen could account for the low

424 degradation efficiency in O_2-saturated condition.

425         $DMB + h\nu \rightarrow {}^1DMB^* \rightarrow {}^3DMB^*$ (R1)

426         ${}^3DMB^* \rightarrow DMB$ (R2)

427         ${}^3DMB^* \rightarrow Products$ (R3)

428         ${}^3DMB^* + {}^1DMB^* \rightarrow DMB^{\bullet+/\bullet-}(DMB^{\bullet+} + DMB^{\bullet-})$ (R4)

429         ${}^3DMB^* + O_2 \rightarrow DMB + {}^1O_2$ (R5)

430         $DMB^{\bullet-} + O_2 \rightarrow \cdot DOM^+ + O_2^{\bullet-}$ (R6)

431         $O_2^{\bullet-} + 2H^+ \rightarrow H_2O_2 + O_2$ (R7)

432 $H_2O_2 \rightarrow 2OH$ (R8)
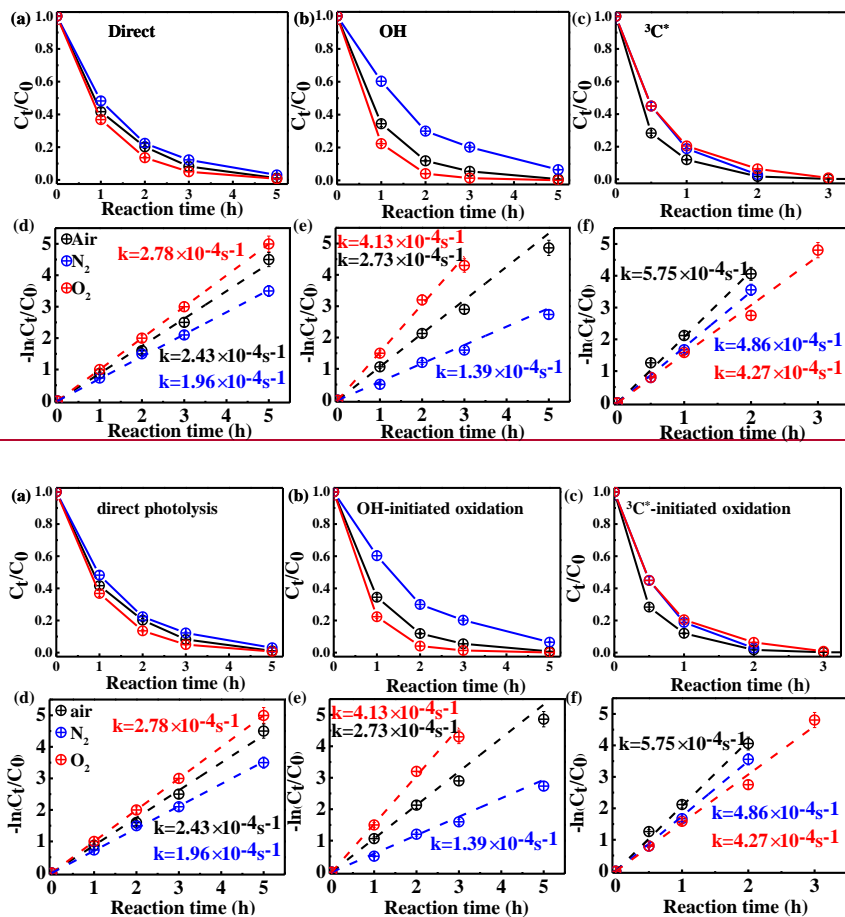
Figure 3. Ratio of unreacted eugenol concentration to its initial concentration (C_t/C_0) as a function of reaction time at different saturated gases under (a) direct photolysis (b) OH-initiated oxidation and (c) $^3C^*$-initiated oxidation. Rate constants of (a-c) are presented in (d-f) correspondingly.

3.2.4 Variations of pH and dissolved oxygen

The initial pH values of reaction solutions for direct photolysis and OH-initiated oxidation were unadjusted, while that for the $^3C^*$-oxidation was adjusted to 3. The variation of solution pH is presented in Fig. 4a. The pH values decreased quickly at the beginning of illumination (from 7.4 to ~5.0 in the first 1 hour) then tended to be flat for

both direct photolysis and OH-initiated oxidation. However, little change of pH (less than 0.1 unit) was observed for the $^3C^*$-initiated photooxidation throughout the oxidation, which can be likely ascribed to its low initial pH of 3. Since the solution pH was acidic (pH=3), we cannot rule out formation of acidic products (such as organic acids) during $^3C^*$-initiated oxidation as during direct photolysis and OH-initiated oxidation.

As discussed in Section 3.2.3, oxygen can take part in photochemical reaction to form ROS, which may in turn destroy the structure of precursor. Here we measured the oxygen consumption during oxidation through determination of dissolved oxygen (DO) contents by a dissolved oxygen meter (Seven2Go Pro S9, Zurich, Switzerland). DO was consumed mainly at the first 1 hour and remained stable afterwards (Figs. 4b-c and Fig. S5). The amounts of consumed DO followed the order of $^3C^*$>OH>direct photolysis. The maximum consumed DO was found in $^3C^*$-initiated oxidation, which might be explained by the consumption of O_2 that reacts with $^3C^*$ form $^1O_2$ (R5). Obviously, a steady-state DO level was reached when the consumption rate was equal to the diffusion of O_2 into the solution (Pan et al., 2020). Overall, these results re-emphasize that O_2 can influence eugenol degradation and chemical transformation via induction of radical chain reactions.
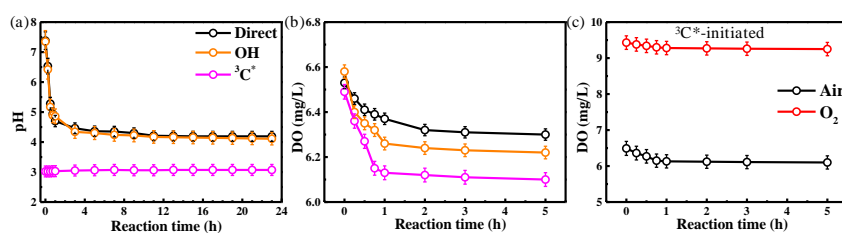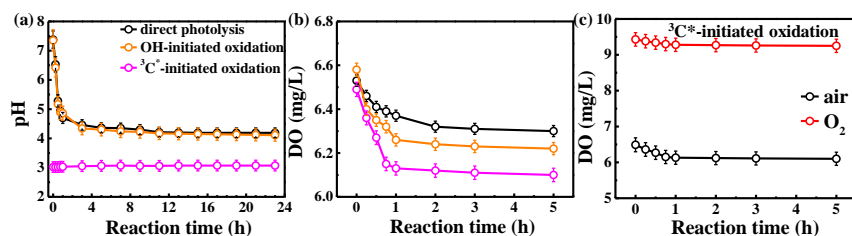
Figure 4. (a) pH values and (b) dissolved oxygen (DO) contents against reaction time under direct photolysis, OH-initiated oxidation, $^3C^*$-initiated oxidation, and (c) DO contents during $^3C^*$-initiated oxidation under air or O_2-saturated conditions.

3.3 Optical properties of reaction products

3.3.1 Light-absorbing properties

The UV-vis light absorption spectra of the solutions at different reaction times are presented in Fig. 5. The light absorption by eugenol itself mainly occurs in the range of 260-300 nm (n→π* electronic transition, 270-350 nm), which overlaps with the major photon fluxes (280 and 500 nm) of our lamp for photooxidation. Therefore, we can clearly observe that the characteristic absorption peak at 280 nm of precursor decreased with the propagation of direct photolysis (Fig. 5a), similar to that in OH-initiated photooxidation (Fig. 5b). However, the reaction was quick in the presence of $^3C^*$, and the characteristic absorption peak at 280 nm after 3 hours of illumination almost disappeared, suggesting nearly a complete loss of eugenol, consistent with the results in Section 3.1 that more than 99% eugenol was degraded in 3 hours. Additionally, there was an obvious absorption enhancement at longer wavelengths (300-400 nm) during the photooxidation, whereas eugenol itself did not absorb light in this range, indicating some light-absorbing products (e.g., brown carbon (BrC) species) were generated. Aqueous photooxidation of some phenolic compounds (e.g., vanillic acid) also presented long-wavelength (300-400nm) light absorbance, with intensity increasing

with illumination time (Tang et al, 2020; Zhao et al., 2015). In addition, there were some differences for light absorbance at wavelength of 300-400 nm in the three reaction conditions. For direct photolysis and OH-initiated oxidation, light absorbance increased during the first 15 hours, then remained at a plateau until 23 hours. However, for $^3C^*$-initiated oxidation, light absorbance increased during the first 7 hours, then decreased slowly afterwards. The different shapes of UV-vis spectra between OH and $^3C^*$ photooxidations indicate formations of different products.

Compared to the light spectrum of eugenol, there were also increases of light absorbance at ~260 nm ($\pi \to \pi^*$ electronic transitions) upon aqueous oxidation in all three reaction conditions (Fig. 5), demonstrating the generation of new substances likely with both aromatic C=C and carbonyl (C=O) functional groups (Tang et al., 2020). The enhancement at 300-400 nm may point to products with high MWs and conjugated structures. Unfortunately, we were unable to quantify the relative contributions of individual products to the overall light absorbance between 300 to 400 nm due to lack of a full speciation of the products and their light absorption spectra.
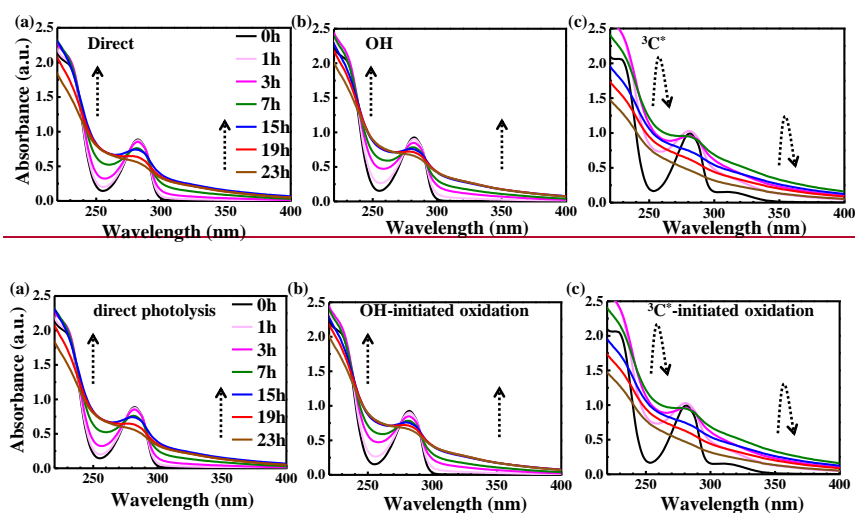

Figure 5. UV–vis light absorption spectra of reacted solutions at different reaction times under (a)

24

502   direct photolysis, (b) OH-initiated oxidation, and (c)^{3}C*-initiated oxidation.

503   **3.3.2 Fluorescence properties**

504   The fluorescence properties of solutions before (0 hour) and during photooxidation

505   (3 and 7 hours) were investigated via the EEM technique, as shown in Fig. 6. For

506   comparison, we also presented EEM profiles of pure eugenol (non-irradiated), pure

507   DMB, and the end solutions (23 hours) of direct photolysis and OH-initiated oxidation

508   in Fig. S6. The peaks at Excitation/Emission (Ex/Em)=275/313 nm can be attributed to

509   fluorescence of the phenolic structure of parent substance (eugenol here), as suggested

510   by Laurentiis et al. (2013). As shown in both Fig. 6 and Fig. S6, the fluorescence

511   intensity decreased after oxidation due to eugenol decay, and the reduction was very

512   fast for ^{3}C*-initiated oxidation. This finding matches with the fast degradation and large

513   rate constant for ^{3}C*-initiated oxidation. The EEM plots for direct photolysis and OH-

514   initiated oxidation had similar contour patterns as shown in Figs. 6a and b, although

515   EEM profiles changed significantly with irradiation time. We also observed distinct

516   fluorescent peaks at Ex/Em=235/(400-500) nm, indicating that illumination can cause

517   a red shift in fluorescence emission wavelength. As suggested by Chang et al. (2010),

518   fluorophores at Ex/Em=240/400 nm are linked with aromatic structures and condensed

519   saturated bonds including polycyclic aromatic hydrocarbons. Another work (Li et al.,

520   2021) showed that red shift in the fluorescence spectra was usually related to an

521   increase in the size of ring system and an increase in the degree of conjugation. Previous

522   studies (Chen et al., 2016a; Chen et al., 2019) have reported that fluorescent compounds

523   with emission wavelength at 400-500 nm were likely linked with HULIS. Additionally,

524   HULIS have two typical fluorescent peaks in EEM profile at Ex/Em=(200-300)/(400-

525   500) nm and Ex/Em=350/(400-500) nm with the former one having a higher intensity

526   (Graber and Rudich, 2006; Laurentiis et al., 2013; Vione et al., 2019). There was also

527   evidence that direct photolysis of tyrosine and 4-phenoxyphenol generated HULIS with

528   new fluorescence signals at Ex/Em=(200-250)/(400-450) nm and 300/(400-450) nm

529   (Bianco et al., 2014). In this regard, we inferred that new peak at Ex/Em=235/(400-500)

530   nm here was likely attributed to HULIS. For the $^3C^*$-initiated oxidation, extra

531   fluorescent peaks at Ex/Em=(220-300)/(400-500) nm appeared in the first 1 hour (data

532   not shown), but their intensities weakened and gradually disappeared upon prolonged

533   reactions (3 hours). Nevertheless, EEM results should be interpreted with caution

534   because many substances might contribute to absorption and emission at a certain

535   wavelength, and it is hard to distinguish and isolate fluorescent and nonfluorescent

536   constituents simply via the EEM technique.

537   Another interesting finding was that a small fluorescence peak appeared at

538   Ex/Em=(300-350)/(300-350) nm in some of the EEM profiles. Specifically, it appeared

539   earlier for $^3C^*$-oxidation (at 3 hours) than the other two systems, yet its intensity seemed

540   to be a bit stronger in the end solutions of direct photolysis and OH-oxidation (Fig. S6).

541   Moreover, as suggested by Leenheer and Croue (2003), fluorescence peak position of

542   the maximum Ex/Em for HULIS with lower MWs would shift towards lower

543   wavelengths, thus, we inferred fluorescence peak at Ex/Em=(300-350)/(300-350) nm

544   might be in part attributed to the organic acids with a few carbon atoms (probably C_1-

545   C_6). Nevertheless, large uncertainties still exist in using EEM fluorescence technique

546   to identify molecular compositions of the products due to lack of standard EEM profiles

547   for specific compounds from aqueous phase oxidation and clearly more studies are
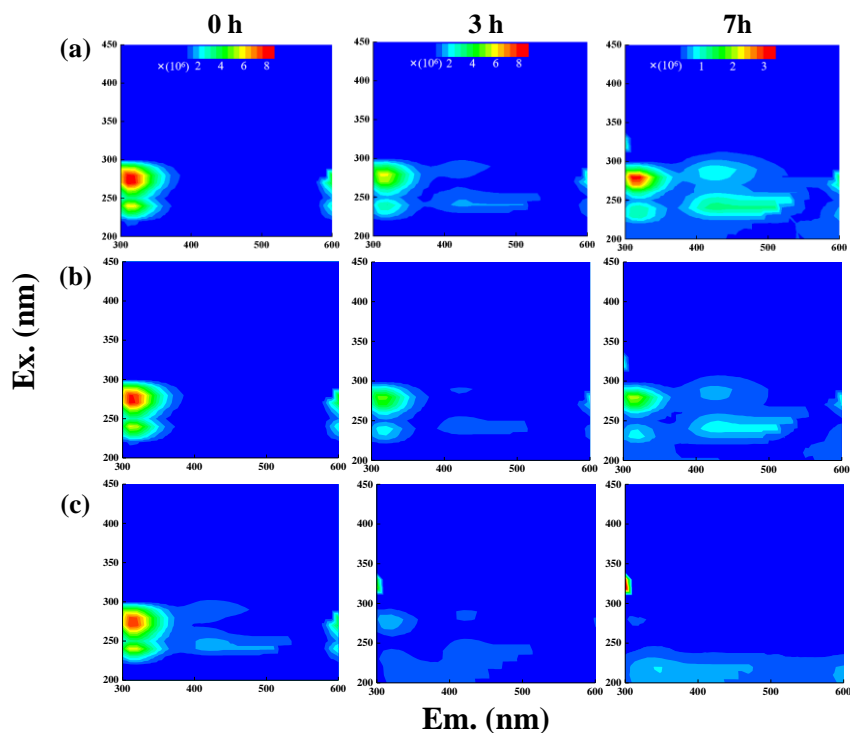
548   needed in future.

Figure 6. EEM fluorescence spectra of the initial solution (0 hour) and those at different reaction time (3 and 7 hours) under (a) direct photolysis, (b) OH-initiated oxidation, and (c) ^{3}C*-initiated oxidation.

3.4 Characteristics of HULIS

The EEM spectra revealed new prominent fluorescent peak at Ex/Em=250/(400-500) nm, which was likely owing to HULIS. HULIS can be divided into fulvic acid (water soluble at all pHs), humic acid (base soluble, acid insoluble) and humin (insoluble at all pHs). In principle, extracted HULIS in this work with polymer-based HLB SPE packing include LMW organic acids, fulvic acids and other humic substances.

Figure 7 presents the measured HULIS concentrations against the reaction time. The results show clearly that aqueous-phase eugenol oxidation is a source of HULIS,

561 and the amount increased gradually in the first 7 hours, then remained at a similar level

562 (about 30 mg/L) for the OH-initiated oxidation. For direct photolysis, HULIS

563 concentration increased until 11 hours and then became steady at a level around 40

564 mg/L. For the $^3C^*$-oxidation, HULIS concentration increased to a maximum at 7 hours,

565 then declined slightly afterwards. A plausible reason of such variabilities is that

566 generated HULIS was capable of further taking part in photochemical reactions since

567 it can act as photosensitizer. Moreover, Yu et al. (2016) characterized the products from

568 aqueous oxidations of phenols by $^3C^*$ triplet states and OH radicals, and found both

569 could produce oligomers and hydroxylated species but the $^3C^*$-oxidation could produce

570 more of these compounds when 50% of the precursor was reacted. Considering the

571 large increases of HULIS in the first 7 hours and the much faster increase of $^3C^*$-

572 oxidation in the first 3 hours shown in Fig. 7, we postulate that HULIS species might

573 be some of the high MW oligomers, which can in turn ~~contributed~~contribute to

574 fluorescence at emission of ~400 nm (Barsotti et al., 2016).

575
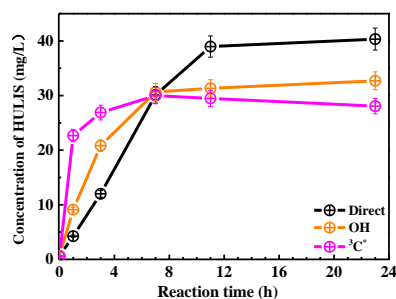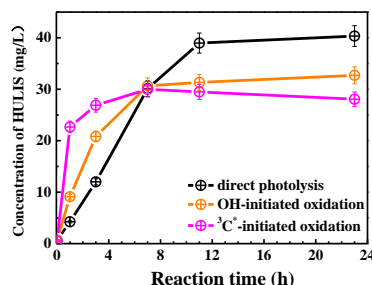
Figure 7. HULIS concentrations as a function of reaction time under direct photolysis, OH-initiated oxidation and $^3C^*$-initiated oxidation.
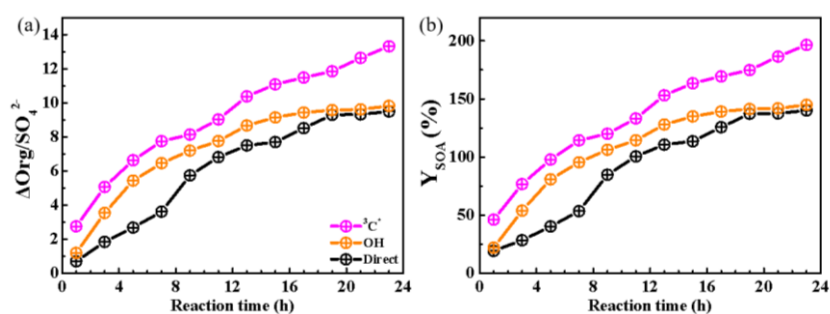
3.5 Mass yield and oxidation degree of reaction products

3.5.1 Mass yields

HULIS is only a subset of the products from aqueous oxidation, and here we used AMS to further quantify the total reaction products. Figure 8a shows SP-AMS measured organic mass profiles (normalized by sulfate mass, $\Delta Org/SO_4^{2-}$) against the reaction time. As the reaction propagated, $\Delta Org/SO_4^{2-}$ increased continuously in $^3C^*$-initiated system. Nevertheless it arose stepwise and reached a maximum at 19 hours, then remained at a plateau for the direct photolysis and OH-mediated oxidation. Figure 8b illustrates the calculated mass yields at different reaction times. The mass yields were in the ranges of 46.2%-196.5%, 22.1%-144.9%, 19.3%-140.1% for $^3C^*$-oxidation, OH-oxidation and direct photolysis, respectively. For the same oxidation time, mass yield from $^3C^*$-oxidation was generally higher than those from OH-oxidation and direct photolysis. There are two plausible reasons for high mass yield of $^3C^*$-initiated oxidation. First, oxidation by $^3C^*$ was more efficient to form oligomers and functionalized/oxygenated products (Richards-Henderson et al., 2014; Yu et al., 2016). Higher oxidative degree of products from $^3C^*$-initiated photooxidation (see Sec.3.5.2)

supports this hypothesis. Secondly, more light-absorbing products formed during initial

stage of $^3C^*$-oxidation (Fig. 5c) may accelerate oxidation by acting as photosensitizers

(Tsui et al., 2018).

The product mass yields obtained in this work (~20%-197%) overall agree with

those reported previously for phenolic compounds. For examples, Huang et al. (2018)

reported mass yields of 30-120% for syringaldehyde and acetosyringone; Smith et al.

(2014) found that mass yields of aqSOA from three phenols with $^3C^*$ were nearly 100%,

and Ma et al. (2021) reported a yield ranging from 59 to 99% for six highly substituted

phenols with $^3C^*$; Mass yields of SOA from three benzene-diols were near 100% with

both OH and $^3C^*$ oxidants (Smith et al., 2015); Direct photolysis of phenolic carbonyls,

and oxidation of syringol by $^3C^*$, had SOA mass yields ranging from 80 to 140% (Smith

et al., 2016). Our previous study on eugenol OH oxidation illuminated by a 500 W Xe

lamp reported a mass yield of ~180% (Ye et al., 2020), slightly higher than the value

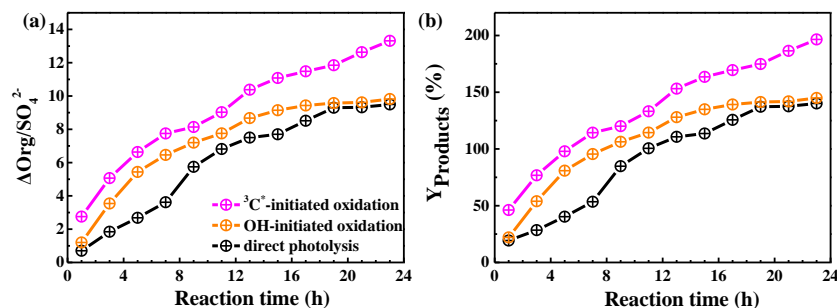determined here owing to different light wavelengths/intensities.

Figure 8. Variations of the organic mass normalized by sulfate (a) ($\Delta Org/SO_4^{2-}$) and (b) mass yields of reaction products with reaction time under direct photolysis, OH-initiated oxidation and $^3C^*$-initiated oxidation.

3.5.2 Oxidation degree

In order to further probe oxidation levels of the reaction products, O/C derived from SP-AMS mass spectrum of the organics was used to represent the oxidation degree of products. In addition, carbon oxidation state (OSc, defined as 2*O/C - H/C) (Kroll et al., 2011) was also calculated. Figures 9a-c depict variations of the elemental ratios (O/C and H/C) and OSc during oxidations. ~~Dramatic~~Rapid increases of O/C and OSc during the initial stage of oxidation (within 1 hour) were observed, with O/C changing from 0.26 to 0.65, from 0.26 to 0.70, from 0.25 to 0.75, as well as OSc from -1.11 to -0.15, from -1.16 to -0.05, from -1.13 to 0.09 for direct photolysis, OH-oxidation and $^3C^*$-oxidation, respectively. The O/C was lower than those of other phenolic aqSOA (Yu et al., 2014) due to different substituted groups in aromatic ring of the precursors. Both O/C and OSc gradually increased, while H/C changed little after 1 hour. The enhancements of OSc in the end were 1.22, 1.11 and 0.86 for $^3C^*$-initiated oxidation, OH-initiated oxidation and direct photolysis, respectively.

Furthermore, the f_{44} vs. f_{43} diagram ("triangle plot") can be used to demonstrate

the evolution of SOA during oxidation (Ng et al., 2010). The f_{44} and f_{43} are defined as the ratios of signal intensities of m/z 44 (mainly CO_2^+) and 43 (mainly $C_2H_3O^+$) to the total organics. The results that the f_{44} increased continuously (moved upwards) during both OH and $^3C^*$ oxidations, indicating persistent formation of highly oxygenated compounds including organic acids, such as formic acid and oxalic acid (Sun et al., 2010). Note the f_{44} enhancement was much more significant for $^3C^*$ oxidation (from 0.07 to 0.16) than direct photolysis (from 0.07 to 0.12) and OH oxidation (from 0.07 to 0.13), consistent with ~~the behaviors of~~ its higher O/C and OSc. The f_{43} value decreased in the first stage (1-3 hours) and then increased at later stages. The final f_{43} values were almost the same as those of the initial solutions and were small. As a result, all data points located outside the f_{44} vs. f_{43} region (bounded by the two dash lines in Figs. 9d-f) for ambient aerosols established by Ng et al. (2010).

In summary, our results shown here demonstrate that aqueous phase eugenol photochemical oxidation can generate highly oxygenated products and hence increase the degree of oxygenation of overall SOA.
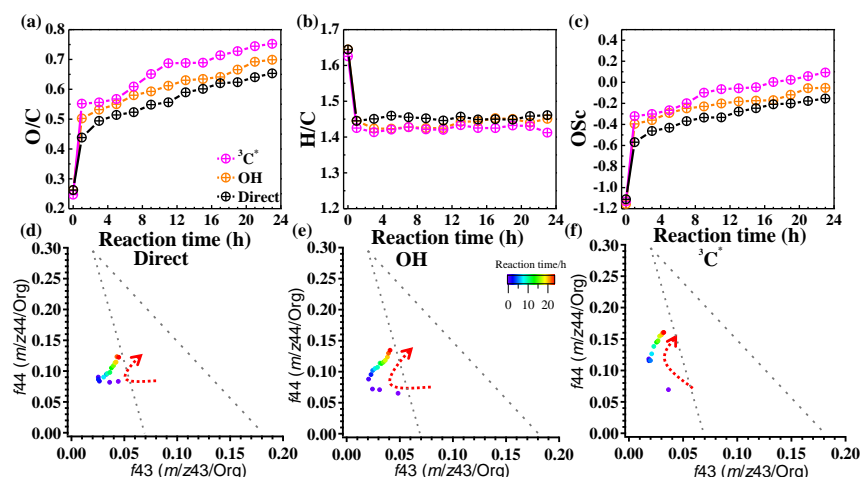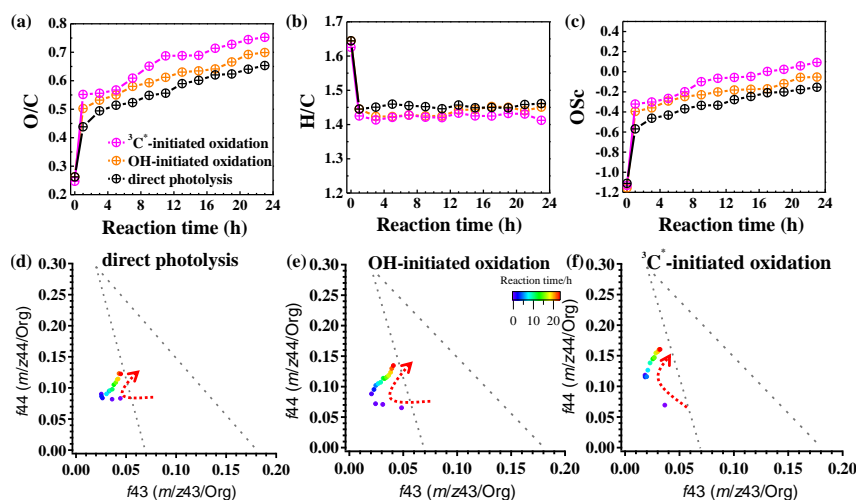
Figure 9. Variations of the elemental ratios of (a) O/C, (b) H/C and (c)oxidation state (OSc) as a function of reaction time; f_{44} vs. f_{43} plots of reaction products under (d) direct photolysis, (e) OH-initiated oxidation, and (f) $^3C^*$-initiated oxidation.

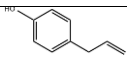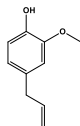## 3.6 Molecular characterization of reaction products and proposed reaction mechanism
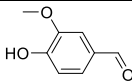
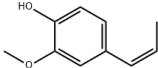### 3.6.1 Major products identified by GC-MS
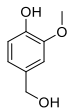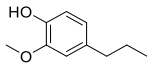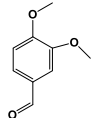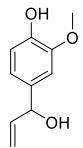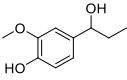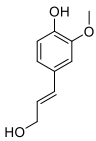
SP-AMS was limited to probe bulk composition of low-volatility oxidation products, thus the molecular-level characterization of products was performed by using GC-MS here. The total ion chromatograph (TIC) of GC-MS on the solutions before illumination (0 hour) and at illumination times of 11 and 23 hours for the $^3C^*$-initiated photooxidation is shown in Fig. S7. As shown in Fig.S7, eugenol (retention time (RT) at 11.50 min) loss was more than 90% at 11 hours, which could be c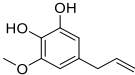onfirmed by the experimental data reported in Section 3.1. Comparison of products at 11 hours and 23 hours showed no significant difference. Similar to aqueous photochemical oxidation

661 with OH (Ye et al., 2020), a series of products were identified and listed in Table 2.

662 Except 5-ally-3-methoxybenzene-1,2-diol (MW 180, RT=12.59 min), the other eight

663 products were detected for both OH and $^3C^*$-initiated photooxidations. Some of them

664 (Eugenol, DMB, product 1, 2, 5) were identified by using certified reference materials,

665 some of them (product 3, 4, 6, 7, 8, 9) were inferred according to the molecular ion

666 peaks and fragments from GC-MS, based on spectra from the NIST database (Stein,

667 2014) and on the reactants and reaction conditions.

668 We also found 4-(1-hydroxypropyl)-2-methoxyphenol (product 8) was relatively

669 abundant (Fig.S7), suggesting functionalization might ~~dominates~~dominate as compared

670 to oligomerization and fragmentation. Products were mainly from addition/elimination

671 of hydroxyl (-OH), methoxyl (-OCH$_3$) to benzene ring or allyl group and further

672 oxidized to carbonyl or carboxyl compounds. As suggested by Bonin et al. (2007), the

673 OH-addition to the aromatic ring of phenol preferentially takes place at the ortho (48%)

674 and the para (36%) positions, leading to the formation of OH-adduct product 6 (5-allyl-

675 3-methoxybenzene-1,2-diol). Notably, dimers and ring-opening products were not

676 observed, but they cannot be excluded since they would be probably out of the detection

677 of GC-MS technique (Vione et al., 2014).

678
679 **Table 2.** Major reaction products identified via GC-MS

	RT (min)	Name*	Proposed chemical structure	Chemical formula	Nominal MW (g/mol)
Product 1	10.68	4-allylphenol		C$_9$H$_{10}$O	134
Precursor	11.50	Eugenol		C$_{10}$H$_{12}$O$_2$	164

Product 2	11.81	4-hydroxy-3-methoxybenzaldehyde		$C_8H_8O_3$	152
Product 3	12.06	(E)-2-methoxy-4-(prop-1-en-1-yl)phenol		$C_{10}H_{12}O_2$	164
Product 4	12.11	4-(hydroxymethyl)-2-methoxyphenol		$C_8H_{10}O_3$	154
Product 5	12.18	2-methoxy-4-propylphenol		$C_{10}H_{14}O_2$	166
Photosensitizer	12.29	3,4-dimethoxybenzaldehyde(DMB)		$C_9H_{10}O_3$	166
Product 6**	12.59	5-allyl-3-methoxybenzene-1,2-diol		$C_{10}H_{12}O_3$	180
Product 7	12.65	4-(1-hydroxyallyl)-2-methoxyphenol		$C_{10}H_{12}O_3$	180
Product 8	12.79	4-(1-hydroxypropyl)-2-methoxyphenol		$C_{10}H_{14}O_3$	182
Product 9	12.91	(E)-4-(3-hydroxyprop-1-en-1-yl)-2-methoxyphenol		$C_{10}H_{12}O_3$	180

680   *Precursor (eugenol) and triplet precursor (DMB) are also shown.

681 **This compound was only identified in ^{3}C*-oxidation solution.

3.6.2 Reaction mechanism

683   The reaction pathways of ^{3}C*-initiated photooxidation of eugenol are

684 demonstrated in Scheme 1 based on the products identified by GC-MS. The

685 other intermediates and the potential pathways were proposed according to the

686 identified products and the reaction rationality from the starting reactant. To better

687 depict the mechanism, DMB was expressed as [RCHO] and eugenol as Ph-R for

688 simplicity. [RCHO] absorbs light and undergoes excitation to ^{1}[RCHO]*, then

689 experiences the intersystem crossing (ISC) to form ^{3}[RCHO]*. ^{3}[RCHO]* can

690 participate in subsequent reactions via three channels. First, it can react with O_2 to form

691 $^1O_2$ via energy transfer. Secondly, it can transform to [RCHO]$^{•-}$, subsequently reacts

692 with O_2 to generate $O_2^{•-}$ via electron transfer, which can disproportionate to H_2O_2. The

693 decomposition of H_2O_2 can generate OH radical. Thirdly, the ^{3}[RCHO]* can react with

694 Ph-R to from [Ph-R•] via H-abstraction. The cleavage of [Ph-R•] to free radical segment

695 (such as CH$_2$CH• or CH$_3$O•) takes place, then an additional hydrogen transfer could

696 occur, resulting in a 2H-addition to the new intermediate to form 4-allyl-phenol

697 (product 1). Similarly, when the CH$_2$CH• is lost from [Ph-R•], an addition of H_2O

698 would happen on the new compound (product 4) and further oxidized to 4-hydroxy-3-

699 methoxybenzaldehyde (product 2). Another possibility is the intermediate [Ph-R•] can

700 resonate to several different isoelectronic species, the radical position changes to

701 aromatic ring or allyl group site, which would couple with ~~HO•~~ OH to form

702 hydroxylated eugenol monomer (product 6, 7, 9 MW=180). Consequently, the

703 isoelectronic species at allyl group site could also abstract a hydrogen to form

704 isoeugenol (product 3 MW=164). Also, breakage of C=C into C-C and 2H-addition at

36

705 allyl group site could form 2-methoxy-4-propyl-phenol (product 5, MW=166). Besides,

706 the C=C breaking intermediate can couple with ~~HO•~~OH to form 4-(1-hydroxypropyl)-

707 2-methoxyphenol (product 8, MW=182). In conclusion, $^3C^*$ can directly oxidize

708 eugenol to form SOA products or small molecular compounds, or indirectly oxidize

709 eugenol via energy transfer, electron transfer, hydrogen abstraction, proton-coupled

710 electron transfer or other radical chain reactions.

711   The organic groups, such as methoxy, allyl groups can be eliminated from

712 aromatic ring, which then participate in photochemical reaction, resulting in generation

713 of dimers, small organic acids, CO_2 and H_2O, etc. Dimers previously reported from

714 aqueous reaction of 4-methylsyringol with OH were not detected via GC-MS in the

715 present work but dimer fragment ions ($C_{20}H_{22}O_4^+$) were detected by SP-AMS with trace

716 amounts. Functionalization due to the additions of hydroxyl, carbonyl functional groups

717 to the aromatic rings could account for the enhancement of light absorption at

718 wavelength of 300-400 nm. However, polar high MW organic acids were not detected

719 likely due to the limitation of GC-MS technique.

720
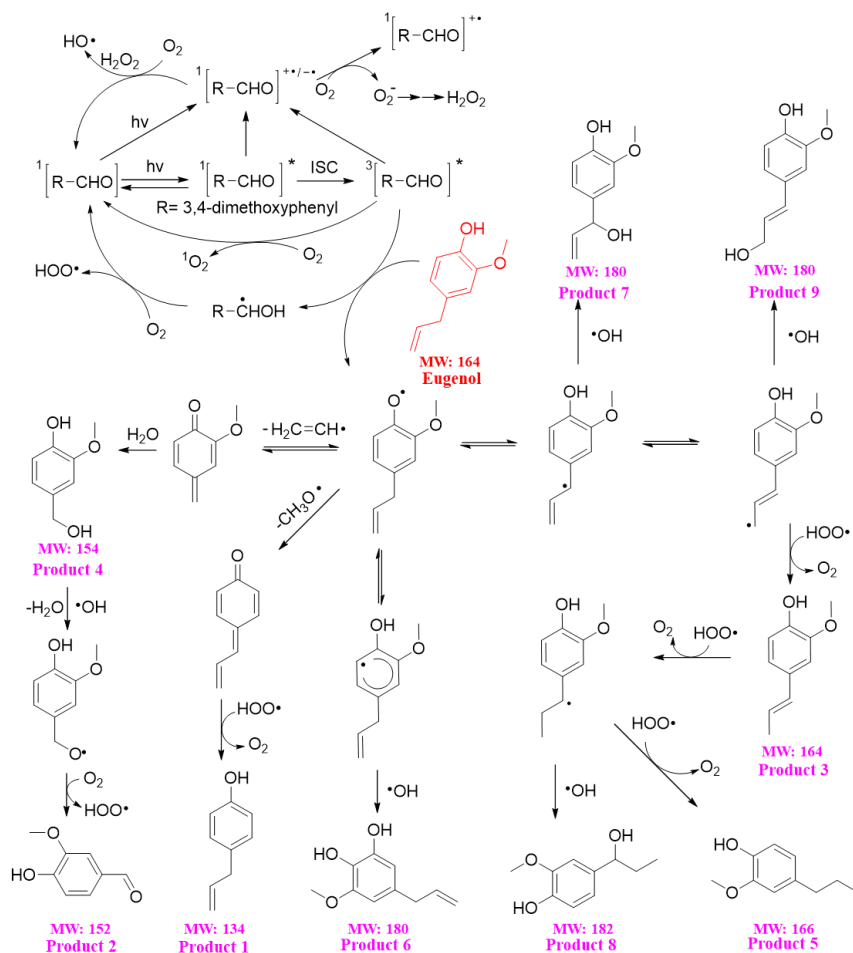
Scheme 1. Proposed reaction mechanism of $^3C^*$-initiated photooxidation of eugenol. The red text represents the precursor, and the compounds labeled by Product 1-9 are those identified by GC-MS (Table 2).

3.7 Oxidative potential (OP) of reaction products

The OP of oxidation products can be represented by the consumption rate of DTT concentration, defined as R_{DTT}. Figure 10a shows the DTT consumed mass (M_{DTT}) as a function of incubation times (0, 30, 60, 90, 120 and 150 min) for a triplicate sample

728 (300 μM eugenol) and blank (ultrapure water). M_{DTT} values for both blank and eugenol

729 were proportional to incubation time, indicating that ROS-generating substances in

730 reaction solution act only as catalyst and itself was not consumed. The slopes represent

731 DTT consumption rates, which are also illustrated in Fig. 10a. Average R_{DTT0} (blank)

732 was 0.31 μM/min and R_{DTT} for initial 300 μM eugenol (before experiment) was 0.52

733 μM/min. Since self-oxidation of DTT might lead to the consumption of DTT in

734 ultrapure water, final DTT consumption rate of reacted solution after oxidation was then

735 blank-corrected by subtracting the average R_{DTT0}.

736 Figure 10b shows changes of blank-corrected R_{DTT} with reaction time for direct

737 photolysis, OH-initiated oxidation and $^3C^*$-initiated oxidation, respectively. The R_{DTT}

738 value of $^3C^*$-oxidation products increased quickly and reached the maximum (0.9) at 7

739 hours, then decreased slowly and its end value was lower than that from OH-oxidation.

740 The R_{DTT} value of OH-oxidation products on the other hand increased slowly and

741 reached the maximum at 21 hours. The R_{DTT} value of products from direct photolysis

742 increased continuously but also slowly to ~0.36 till the end of oxidation. Nevertheless,

743 we can see that the final R_{DTT} values were all higher than that of eugenol, proving that

744 aqueous-phase processing can generate products with higher OP, resulting in more

745 health hazards than the precursor does. The DTT consumption rates are comparable to

746 those using the same DTT method (Charrier and Anastasio, 2012; Lin and Yu, 2019).

747 The weak correlation was found between HULIS concentration and R_{DTT}, implying that

748 OP was not only dependent upon HULIS. Moreover, HULIS with diverse molecular

749 structures also exhibit different ROS-generation potentials (Kramer et al., 2016),

750 therefore the HULIS as an ensemble may not correlate well with OP.
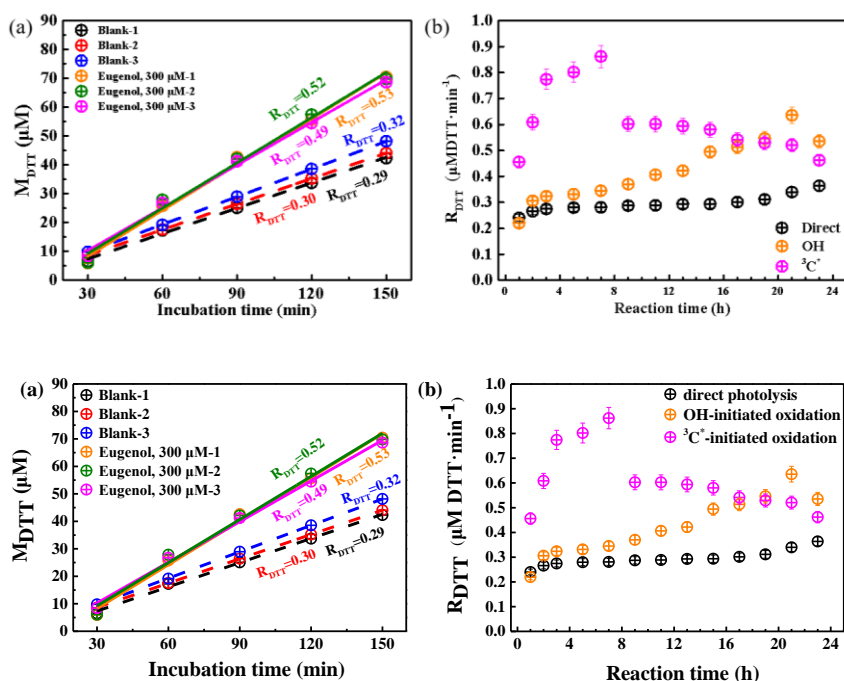
Figure 10. (a) DTT consumed mass versus incubation times for blank (ultrapure water) and 300 μM eugenol solutions in a triplicate, and (b) blank-corrected DTT consumption rates versus reaction time for direct photolysis, OH-initiated oxidation and $^3C^*$-induced oxidation.

4. Atmospheric implications

The high mass yields of aqueous-phase photooxidation of eugenol (exceeding 100% after 23 hours of illumination) found here are similar or even higher than those previously reported yields of a number of phenolic compounds (e.g., Smith et al., 2014, 2015, 2016; Ma et al., 2021), which re-emphasizes the importance of biomass burning (BB) to SOA budget (Gilardoni et al., 2016), particularly in regions or periods with significant BB activities. In addition, our study here used 300 μM H_2O_2 and 15 μM DMB as sources of OH and $^3C^*$, and $^3C^*$-mediated oxidation appeared to be faster than

40

764   OH-initiated oxidation of eugenol. Of course, whether or not $^3C^*$ is more important

765   than OH in real atmosphere depends upon their concentrations. OH and $^3C^*$ are difficult

766   to measure and concentrations vary greatly in real atmospheric samples. Herrmann et

767   al. (2010) estimated an average OH level of 0.35×10^{-14} M in urban fog water; Kaur and

768   Anastasio (2018) measured $^3C^*$ concentration to be $(0.70\text{-}15) \times 10^{-14}$ M, 10-100 times

769   higher than the co-existing OH in ambient fog waters; Kaur et al. (2019) determined

770   both OH and $^3C^*$ concentrations in PM extracts, OH steady-state concentration was

771    $4.4(\pm 2.3) \times 10^{-16}$ M, similar to its level in fog, cloud and rain, while $^3C^*$ concentration

772   was $1.0(\pm 0.4) \times 10^{-13}$ M, a few hundred times higher than OH and nearly double its

773   average value in fog. Therefore, together with these measurements, our findings signify

774   a likely more important role of $^3C^*$ than OH in aqueous-phase (especially aerosol water)

775   reactions. However, the liquid water content of aerosol is typically ~10000 times

776   smaller than that of cloud (for instance, ~50 μg m^{-3} versus 0.5 g m^{-3}). Even if the

777   reaction rates in aerosol water were 10 times higher than those in cloud water, the

778   overall importance of aqueous reactions initiated by the same oxidant in aerosol phase

779   would be still ~1000 times smaller than it in cloud water. Moreover, quenching

780   experiments reveal that O_2 can inhibit eugenol degradation by effectively scavenging

781    $^3C^*$ while it can promote degradation by fostering chain reactions in OH-induced

782   oxidation, which offer insights to the control of reaction pathways by regulating ROS

783   generations; of course, such operation calls for application of highly sensitive EPR

784   method.

785   Eugenol has a strong light absorption peak around 280 nm, therefore it can undergo

786   direct photolysis, and addition of OH or other photosensitizers ($^3C^*$) can gradually

787   diminish its light absorption around 280 nm, but increase the absorption in visible light

788   range (>300 nm). In the meantime, HULIS was generated continuously, and GC-MS

identified a number of high MW organic products, in line with those detected in earlier aqueous photooxidation of phenolic compounds (Jiang et al., 2021; Misovich et al., 2021; Tang et al., 2020; Yu et al., 2014). Overall, our work demonstrates that aqueous oxidation of BB emissions is a source of BrC, and this BrC may act as photosensitizer to oxidize other species; a portion of this BrC might be HULIS, and some high MW aromatic compounds are a subset of this HULIS. However, a recent study by Wang et al. (2021) shows that fossil ~~foil~~fuel derived OA (FFOA) can be an effective precursor of aqSOA, but the aqSOA became less light-absorbing than the FFOA. These contrasting results indicate that contribution of aqueous oxidation to BrC is largely dependent upon the precursors; molecular structures of major chromophores, changes of the structures upon oxidation as well as their interplay with light absorptivity should be carefully investigated to achieve a full understanding of the impacts of aqueous processing on air quality, radiative forcing and climate change.

Investigations on the OPs of reaction products from eugenol photooxidation show that aqueous processing can produce more toxic products than the precursor. This result is in agreement with our previous work on resorcinol, hydroquinone and methoxyhydroquinone (Ou et al., 2021). Although more studies on a broad spectrum of atmospherically relevant species and multiple indicators of toxicity are clearly needed, our findings here underscore the potential of aqueous processing on the enhancement of particle toxicity.

5 Conclusions

This study comprehensively investigated the aqueous photooxidation of eugenol upon direct photolysis and attacks by OH radicals and ^{3}C* triplet states. By using a suite of techniques, the decay kinetics of eugenol, chemical, optical properties as well

813   as toxicity of reaction products were studied. The first-order rate constants followed the

814   order of $^3C^*$>OH >direct photolysis (300 μM H_2O_2 and 15 μM DMB as sources of OH

815   and $^3C^*$). Further quenching experiments on different ROS during $^3C^*$-mediated

816   oxidation showed that $^3C^*$ was the major contributor, followed by $^1O_2$, $O_2^{\cdot-}$ and OH;

817      $O_2^{\cdot-}$ played a more important role than OH during OH-initiated oxidation. The rate

818   constants under saturated O_2, air and N_2 followed the order of $k_{O_2} > k_{Air} > k_{N_2}$ for both

819   direct photolysis and OH-initiated oxidation, but changed to $k_{Air} > k_{N_2} > k_{O_2}$ for $^3C^*$-

820   mediated oxidation. O_2 appeared to be a scavenger of $^3C^*$ therefore suppressing $^3C^*$

821   oxidation while it could promote generation of OH thus accelerate OH-mediated

822   oxidation. pH and DO levels both decreased during oxidation, indicating formation of

823   acids and a certain role of DO in oxidation.

824   Eugenol itself can absorbs lights significantly around 280 nm, and aqueous

825   oxidation gradually decrease this absorption of UV light but enhanced the absorbance

826   in the visible light range (mainly 300-400 nm), indicative of the generation of BrC

827   species. These species were likely linked with HULIS, as HULIS concentration

828   increased during the course of oxidation, in particular for the initial stage of $^3C^*$-

829   mediated reactions. The final mass yields of reaction products (after 23 hours of

830   irradiation) were 140.1%, 144.9% and 196.5% for direct photolysis, OH-oxidation and

831      $^3C^*$-oxidation, respectively. Oxidation degrees of the products increased continuously

832   with the illumination time, indicating persistent formation of highly oxygenated

833   compounds, especially during $^3C^*$-mediated reactions. Molecular characterization by

834   GC-MS identified a series of oxygenated compounds, allowing us to propose the

835   detailed oxidation mechanism. Functionalization appeared to be a dominant pathway to

836   form the observed species.

837   DTT method was used to assess OP of the reaction products. The end products in

all three sets of experiments showed higher DDT consumption rates than that of the precursor; products from ^{3}C*-oxidation showed particularly fast increase in the first few hours of reactions. This result demonstrates that species that are more toxic than its precursors could be produced upon aqueous oxidation, indicative of the potential toxic effects induced by aqueous processing.

Data availability. The relevant data of this study are available at: http://nuistairquality.com/eugenol_data_and_figure

Supplement. The supplement related to this article is available on line at: XXX

Author Contributions: XDL, YT, LWZ, SSM, SPL, ZZZ and NS conducted the experiments. XDL and YT analyzed the data. XDL and ZLY prepared and wrote the paper with contributions from all co-authors. ZLY and XLG reviewed and commented on the paper.

Competing interests. The authors declare that they have no conflict of interest.

Review statement. This paper was xxx

References

Alam, M. S., Delgado-Saborit, J. M., Stark, C., and Harrison, R. M.: Using atmospheric measurements of PAH and quinone compounds at roadside and urban background sites to assess sources and reactivity, Atmos. Environ., 77(3), 24-35, https://doi.org/10.1016/j.atmosenv.2013.04.068, 2013.

Alegría, A. E., Ferrer, A., Santiago, G., Sepúlveda, E., and Flores, W.: Photochemistry of water-soluble quinones. Production of the hydroxyl radical, singlet oxygen and the superoxide ion, J. Photochem. Photobiol. Chem., 127, 57-65, https://doi.org/10.1016/S1010-6030(99)00138-0, 1999.

Arakaki, T., Anastasio, C., Kuroki, Y., Nakajima, H., Okada, K., Kotani, Y., Handa, D., Azechi, S., Kimura, T., Tsuhako, A., and Miyagi, Y.: A general scavenging rate constant for reaction of hydroxyl radical with organic carbon in atmospheric waters, Environ. Sci. Technol., 47, 8196-8203, https://doi.org/10.1021/es401927b, 2013.

Aryal, R., Lee, B. K., Beecham, S., Kandasamy, J., Aryal, N., and Parajuli, K.: Characterisation of road dust organic matter as a function of particle size: A PARAFAC Approach, Water Air Soil Poll.; 226, https://doi.org/10.1007/s11270-014-2289-y, 2015.

Bari, M, A, Baumbach, G., Kuch, B., and Scheffknecht, G.. Wood smoke as a source of particle-phase organic compoundsin residential areas, Atmos. Environ., 43, 4722-4732, https://doi.org/10.1016/j.atmosenv.2008.09.006, 2009.

Barzaghi, P. and Herrmann, H.: A mechanistic study of the oxidation of phenol by OH/NO2/NO$_3$ in aqueous solution, Phys. Chem. Chem. Phys., 4, 3669-3675,

890   https://doi.org/10.1039/B201652D, 2002.

891   Barsotti, F., Ghigo, G., and Vione, D. Computational assessment of the fluorescence emission of

892   phenol oligomers: A possible insight into the fluorescence properties of humic-like Substances

893   (HULIS), J. Photochem. Photobio. A, 315, 87-93,

894   https://doi.org/10.1016/j.jphotochem.2015.09.012, 2016.

895   Bianco, A., Minella, M., De Laurentiis, E., Maurino, V., Minero, C., and Vione, D. Photochemical

896   generation of photoactive compounds with fulvic-like and humic-like fluorescence in aqueous

897   solution, Chemosphere, 111, 529-536, https://dx.doi.org/10.1016/j.chemosphere.2014.04.035,

898   2014.

899   Bonin, J., Janik, I., Janik, D. and Bartels, D. M.: Reaction of the hydroxyl radical with phenol in water

900   up to supercritical conditions, J. Phys. Chem. A, 111(10), 1869-1878,

901   https://doi.org/10.1021/jp0665325, 2007.

902   Canagaratna, M. R., Jimenez, J. L., Kroll, J. H., Chen, Q., Kessler, S. H., Massoli, P., Hildebrandt Ruiz,

903   L., Fortner, E., Williams, L. R., Wilson, K. R., Surratt, J. D., Donahue, N. M., Jayne, J. T., and

904   Worsnop, D. R.: Elemental ratio measurements of organic compounds using aerosol mass

905   spectrometry: characterization, improved calibration, and implications, Atmos. Chem. Phys.,

906   15, 253-272, https://doi.org/10.5194/acp-15-253-2015, 2015.

907   Chang, J. L., and Thompson, J. E.: Characterization of colored products formed during irradiation of

908   aqueous solutions containing H_2O_2 and phenolic compounds, Atmos. Environ., 44, 541-551,

909   https://doi.org/10.1016/j.atmosenv.2009.10.042, 2010.

910   Charrier, J. G., and Anastasio, C.: On dithiothreitol (DTT) as a measure of oxidative potential for ambient

911   particles: evidence for the importance of soluble transition metals, Atmos. Chem. Phys. 12,

912   9321-9333, https://doi.org/10.5194/acp-12-9321-2012, 2012.

913   Chen, H., Ge, X., Ye, Z.: Aqueous-phase secondary organic aerosol formation via reactions with organic

914   triplet excited states—a short review. Curr. Pollut. Rep., 4, 8-12,

915   https://doi.org/10.1007/s40726-018-0079-7, 2018.

916   Chen, Q., Ikemori, F., and Mochida, M.: Light Absorption and excitation-emission fluorescence of urban

917   organic aerosol components and their relationship to chemical structure, Environ. Sci. Technol.,

918   50, 10859-10868, https://doi.org/10.1021/acs.est.6b02541, 2016a.

919   Chen, Q., Miyazaki, Y., Kawamura, K., Matsumoto, K., Coburn, S., Volkamer, R., Iwamoto, Y., Kagami,

S., Deng, Y., Ogawa, S., Ramasamy, S., Kato, S., Ida, A., Kajii, Y., and Mochida, M.: Characterization of chromophoric water-soluble organic matter in urban, forest, and marine aerosols by HR-ToF-AMS analysis and excitation-emission matrix spectroscopy, Environ. Sci. Technol., 50, 10351-10360, https://doi.org/10.1021/acs.est.6b01643, 2016b.

Chen, Q., Wang, M., Wang, Y., Zhang, L., Li, Y., and Han, Y.: Oxidative potential of water-soluble matter associated with chromophoric substances in $PM_{2.5}$ over Xi'an, China, Environ. Sci. Technol., 53, 8574-8584, https://doi.org/10.1021/acs.est.9b01976, 2019.

Chen, Y., Li, N., Li, X., Tao, Y., Luo, S., Zhao, Z., Ma, S., Huang, H., Chen, Y., Ye, Z., and Ge, X.: Secondary organic aerosol formation from $^3C^*$-initiated oxidation of 4-ethylguaiacol in atmospheric aqueous-phase, Sci. Total. Environ., 723, 137953, https://doi.org/10.1016/j.scitotenv.2020.137953, 2020.

Cho, A. K., Sioutas, C., Miguel, A. H., Kumagai, Y., Schmitz, D. A., Singh, M., Eiguren-Fernandez, A., and Froines, J. R.: Redox activity of airborne particulate matter at different sites in the Los Angeles Basin, Environ. Res., 99, 40-7, https://doi.org/10.1016/j.envres.2005.01.003, 2005.

De Laurentiis, E., Sur, B., Pazzi, M., Maurino, V., Minero, C., Mailhot, G., Brigante, M., and Vione, D.: Phenol transformation and dimerisation, photosensitised by the triplet state of 1-nitronaphthalene: A possible pathway to humic-like substances (HULIS) in atmospheric waters, Atmos. Environ., 70, 318-327, https://doi.org/10.1016/j.atmosenv.2013.01.014, 2013.

Dou, J., Lin, P., Kuang, B. Y., and Yu, J.: Reactive oxygen species production mediated by humic-like substances in atmospheric aerosols: enhancement effects by pyridine, imidazole, and their derivatives, Environ. Sci. Technol., 49(11), 6457-6465, https://doi.org/10.1021/es5059378, 2015.

Ervens, B., Turpin, B. J., and Weber, R. J.: Secondary organic aerosol formation in cloud droplets and aqueous particles (aqSOA): a review of laboratory, field and model studies, Atmos. Chem. Phys., 11, 11069-11102, https://doi.org/10.5194/acp-11-11069-2011, 2011.

Fang, T., Verma, V., Bates, J. T., Abrams, J., Klein, M., Strickland, M. J., Sarnat, S. E., Chang, H. H., Mulholland, J. A., Tolbert, P. E., Russell, A. G., and Weber, R. J.: Oxidative potential of ambient water-soluble $PM_{2.5}$ in the southeastern United States: contrasts in sources and health associations between ascorbic acid (AA) and dithiothreitol (DTT) assays, Atmos. Chem. Phys., 16, 3865-3879, https://doi.org/10.5194/acp-16-3865-2016, 2016.

950   Faust, J. A., Wong, J. P., Lee, A. K., and Abbatt, J. P.: Role of aerosol liquid water in secondary organic
951   aerosol formation from volatile organic compounds, Environ. Sci. Technol., 51, 1405-1413,
952   https://doi.org/10.1021/acs.est.6b04700, 2017.
953   Ge, X., Li, L., Chen, Y., Chen, H., Wu, D., Wang, J., Xie, X., Ge, S., Ye, Z., Xu, J., and Chen, M. Aerosol
954   characteristics and sources in Yangzhou, China resolved by offline aerosol mass spectrometry
955   and   other   techniques.   Environ.   Pollut.,   225,   74-85,   https://doi.org/
956   10.1016/j.envpol.2017.03.044, 2017.
957   George, K. M., Ruthenburg, T. C., Smith, J., Yu, L., Zhang, Q., Anastasio, C., and Dillner, A. M.: FT-IR
958   quantification of the carbonyl functional group in aqueous-phase secondary organic aerosol from
959   phenols, Atmos. Environ., 100, 230-237, https://doi.org/10.1016/j.atmosenv.2014.11.011, 2015.
960   Gilardoni, S., Massoli, P., Paglione, M., Giulianelli, L., Carbone, C., Rinaldi, M., Decesari, S., Sandrini,
961   S., Costabile, F., Gobbi, G. P., Pietrogrande, M. C., Visentin, M., Scotto, F., Fuzzi, S., and
962   Facchini, M. C.: Direct observation of aqueous secondary organic aerosol from biomass-
963   burning   emissions,   Proc.   Natl.   Acad.   Sci.   USA.,   113,   10013-10018,
964   https://doi.org/10.1073/pnas.1602212113, 2016.
965   Gligorovski, S., Strekowski, R., Barbati, S., and Vinoe, D.: Environmental implications of hydroxyl
966   radicals (OH), Chem. Rev., 115(24), 13051-13092, https://doi.org/10.1021/cr500310b, 2015.
967   Graber, E. R., and Rudich, Y.: Atmospheric HULIS: how humic-like are they? A comprehensive and
968   critical review, Atmos. Chem. Phys., 6, 729-753, https://doi.org/10.5194/acp-6-729-2006,
969   2006.
970   Guo, Y., Zhang, Y., Yu, G., and Wang, Y., Revisiting the role of reactive oxygen species for pollutant
971   abatement during catalytic ozonation: the probe approach versus the scavenger approach, Appl.
972   Catal. B Environ., 280, 119418, https://doi.org/10.1016/j.apcatb.2020.119418, 2021.
973   Hawthorne, S.B., Krieger M.S., Miller D.J., and Mathiason M.B. Collection and quantitation of
974   methoxylated phenol tracers for atmospheric pollution from residential wood stoves, Environ. Sci.
975   Technol., 23,470-475, https://doi.org/10.1021/es00181a013, 1989.
976   He, L., Schaefer, T., Otto, T., Kroflic, A., and Herrmann, H.: Kinetic and theoretical study of the
977   atmospheric aqueous-phase reactions of OH radicals with methoxyphenolic compounds, J. Phys.
978   Chem. A, 123, 7828-7838, https://doi.org/10.1021/acs.jpca.9b05696, 2019.
979   Herrmann, H.: Kinetics of aqueous phase reaction relevant for atmospheric chemistry, Chem. Rev., 103,

48

980   4691-4716, https://doi.org/10.1021/cr020658q, 2003.

981   Herrmann, H., Hoffmann, D., Schaefer, T., Bräuer, P. and Tilgner, A.: Tropospheric aqueous-phase free-

982   radical chemistry: Radical sources, spectra, reaction kinetics and prediction tools.

983   ChemPhysChem, 11, 3796-3822, https://doi.org/10.1002/cphc.201000533, 2010.

984   Herrmann, H., Schaefer, T., Tilgner, A., Styler, S. A., Weller, C., Teich, M. and Otto, T.: Tropospheric

985   aqueous-phase chemistry: kinetics, mechanisms, and its coupling to a changing gas phase,

986   Chem. Rev., 115(10), 4259-4334, https://doi.org/10.1021/cr500447k, 2015.

987   Hong, J., Han, B., Yuan, N., and Gu, J.: The roles of active species in photo-decomposition of organic

988   compounds by microwave powered electrodeless discharge lamps, J. Environ. Sci. (China), 33,

989   60-68, https://doi.org/10.1016/j.jes.2014.12.016, 2015.

990   Huang, D., Zhang, X., Chen, Z. M., Zhao, Y., and Shen, X. L.: The kinetics and mechanism of an aqueous

991   phase isoprene reaction with hydroxyl radical, Atmos. Chem. Phys., 11, 7399-7415,

992   https://doi.org/10.5194/acp-11-7399-2011, 2011.

993   Huang, D., Zhang, Q., Cheung, H. H. Y., Yu, L., Zhou, S., Anastasio, C., Smith, J. D., and Chan, C. K.:

994   Formation and evolution of aqSOA from aqueous-phase reactions of phenolic carbonyls:

995   comparison between ammonium sulfate and ammonium nitrate solutions, Environ. Sci.

996   Technol., 52, 9215-9224, https://doi.org/10.1021/acs.est.8b03441, 2018.

997   Huo, Y., Guo, Z., Li, Q., Wu, D., Ding, X., Liu, A., Huang, D., Qiu, G., Wu, M., Zhao, Z., Sun, H., Song,

998   W., Li, X., Chen, Y., Wu, T., and Chen, J. Chemical fingerprinting of HULIS in particulate

999   matters emitted from residential coal and biomass combustion, Environ. Sci. Technol., 55, 3593-

1000   3603. https://doi.org/10.1021/acs. est.0c08518, 2021.

1001   Jiang, W., Misovich, M. V., Hettiyadura, A. P. S., Laskin, A., McFall, A. S., Anastasio, C., and Zhang, Q.:

1002   Photosensitized reactions of a phenolic carbonyl from wood combustion in the aqueous phase-

1003   chemical evolution and light absorption properties of aqSOA, Environ. Sci. Technol., 55, 5199-

1004   5211, https://doi.org/10.1021/acs.est.0c07581, 2021.

1005   Kaur, R., and Anastasio, C.: First measurements of organic triplet excited states in atmospheric waters,

1006   Environ. Sci. Technol., 52, 5218-5226, https://doi.org/10.1021/acs.est.7b06699, 2018.

1007   Kaur, R., Labins, J. R., Helbock, S. S., Jiang, W., Bein, K. J., Zhang, Q., and Anastasio, C.: Photooxidants

1008   from brown carbon and other chromophores in illuminated particle extracts, Atmos. Chem.

1009   Phys., 19, 6579-6594, https://doi.org/10.5194/acp-19-6579-2019, 2019.

1010 Kramer, A.J., Rattanavaraha, W., Zhang, Z., Gold, A., Surratt, J.D., and Lin, Y.-H. Assessing the oxidative
1011   potential of isoprene-derived epoxides and secondary organic aerosol, Atmos. Environ., 130,
1012   211-218, https://dx.doi.org/10.1016/j.atmosenv.2015.10.018, 2016.

1013 Kroll, J. H., Donahue, N. M., Jimenez, J. L., Kessler, S. H., Canagaratna, M. R., Wilson, K. R., Altieri,
1014   K. E., Mazzoleni, L. R., Wozniak, A. S., Bluhm, H., Mysak, E. R., Smith, J. D., Kolb, C. E., and
1015   Worsnop, D. R.: Carbon oxidation state as a metric for describing the chemistry of atmospheric
1016   organic aerosol, Nat. Chem., 3, 133-9, https://doi.org/10.1038/nchem.948, 2011.

1017 Laurentiis, E. D., Socorro, J., Vione, D., Quivet, E., Brigante, M., Mailhot, G., Wortham, H., and
1018   Gligorovski, S.: Phototransformation of 4-phenoxyphenol sensitised by 4-
1019   carboxybenzophenone: evidence of new photochemical pathways in the bulk aqueous phase and
1020   on the surface of aerosol deliquescent particles, Atmos. Environ., 8, 569-578,
1021   https://doi.org/10.1016/j.atmosenv.2013.09.036, 2013.

1022 Lee, A. K. Y., Hayden, K. L., Herckes, P., Leaitch, W. R., Liggio, J., Macdonald, A. M., and Abbatt, J. P.
1023   D.: Characterization of aerosol and cloud water at a mountain site during WACS 2010: secondary
1024   organic aerosol formation through oxidative cloud processing, Atmos. Chem. Phys., 12, 7103-7116,
1025   https://doi.org/10.5194/acp-12-7103-2012, 2012.

1026 Leenheer, J. A., and Croue, J. P. Characterizing aquatic dissolved organic matter, Environ. Sci.
1027   Technol., 37, 18A-26A, https://doi.org/10.1021/es032333c, 2003.

1028 Li, F., Tsona, N. T., Li, J., and Du, L.: Aqueous-phase oxidation of syringic acid emitted from biomass
1029   burning: formation of light-absorbing compounds, Sci. Total Environ., 765, 144239,
1030   https://doi.org/10.1016/j.scitotenv.2020.144239, 2021.

1031 Li, Y. J., Huang, D. D., Cheung, H. Y., Lee, A. K. Y., and Chan, C. K.: Aqueous-phase photochemical
1032   oxidation and direct photolysis of vanillin-a model compound of methoxy phenols from biomass
1033   burning, Atmos. Chem. Phys., 14, 2871-2885, https://doi.org/10.5194/acp-14-2871-2014, 2014.

1034 Lim, Y. B., Tan, Y., Perri, M. J., Seitzinger, S. P., and Turpin, B. J.: Aqueous chemistry and its role in
1035   secondary organic aerosol (SOA) formation, Atmos. Chem. Phys., 10, 10521-10539,
1036   https://doi.org/10.5194/acpd-10-14161-2010, 2010.

1037 Lin, M., and Yu, J. Z.: Dithiothreitol (DTT) concentration effect and its implications on the applicability
1038   of DTT assay to evaluate the oxidative potential of atmospheric aerosol samples, Environ.
1039   Pollut., 251, 938-944, https://doi.org/10.1016/j.envpol.2019.05.074, 2019.

1040   Lu, J., Ge, X., Liu, Y., Chen, Y., Xie, X., Ou, Y., Ye, Z., Chen, M. Significant secondary organic aerosol
1041   production from aqueous-phase processing of two intermediate volatility organic compounds.
1042   Atmos. Environ., 211, 63-68, https://doi.org/10.1016/j.atmosenv.2019.05.014, 2019.

1043   Ma, L., Guzman, C., Niedek, C., Tran, T., Zhang, Q. and Anastasio, C.: Kinetics and mass yields of
1044   aqueous secondary organic aerosol from highly substituted phenols reacting with a triplet excited
1045   state, Environ. Sci. Technol., 55(9), 5772-5781, doi:10.1021/acs.est.1c00575, 2021.

1046   Ma, Y., Cheng, Y., Qiu, X., Cao, G., Kuang, B., Yu, J.Z., and Hu, D. Optical properties, source
1047   apportionment and redox activity of Humic-Like Substances (HULIS) in airborne fine
1048   particulates in Hong Kong, Environ. Pollut., 255,113087,
1049   ~~https://doi.org/10.1016/j.envpol.2019.113087,~~https://doi.org/10.1016/j.envpol.2019.113087,
1050   2019.

1051   Mabato, B. R. G., Lyu, Y., Ji, Y., Li, Y., Huang, D., Li, X., Nah, T., Lam, C. H., and Chan, C. K.: Aqueous
1052   secondary organic aerosol formation from the direct photosensitized oxidation of vanillin in the
1053   absence and presence of ammonium nitrate, Atmos. Chem. Phys., 22, 273-293,
1054   https://doi.org/10.5194/acp-22-273-2022, 2022.

1055   McWhinney, R. D., Zhou, S., and Abbatt, J. P. D.: Naphthalene SOA: redox activity and naphthoquinone
1056   gas–particle partitioning, Atmos. Chem. Phys., 13, 9731-9744, https://doi.org/10.5194/acp-13-
1057   9731-2013, 2013.

1058   Misovich, M. V., Hettiyadura, A. P. S., Jiang, W. Q., and Zhang, Q. Molecular-level study of the photo-
1059   oxidation of aqueous-phase guaiacyl acetone in the presence of $^3C^*$: formation of brown carbon
1060   products, ACS Earth Space Chem., 5, 1983-1996,
1061   https://doi.org/10.1021/acsearthspacechem.1c00103, 2021.

1062   Mladenov, N, Alados-Arboledas, L., Olmo, F .J., Lyamani, H., Delgado, A., Molina, A., and Reche, I.:
1063   Applications of optical spectroscopy and stable isotope analyses to organic aerosol source
1064   discrimination in an urban area, Atmos. Environ., 45, 1960-1969, https://doi.org/
1065   10.1016/j.atmosenv.2011.01.029, 2011.

1066   Nau, W. M., and Scaiano, J. C.: Oxygen quenching of excited aliphatic ketones and diketones, J. Phys.
1067   Chem., 100, 11360-11367, https://doi.org/10.1021/jp960932i, 1996.

1068   Ng, N. L., Canagaratna, M. R., Zhang, Q., Jimenez, J. L., Tian, J., Ulbrich, I. M., Kroll, J. H., Docherty,
1069   K. S., Chhabra, P. S., Bahreini, R., Murphy, S. M., Seinfeld, J. H., Hildebrandt, L., Donahue, N.

1070   M., DeCarlo, P. F., Lanz, V. A., Prevot, A. S. H., Dinar, E., Rudich, Y., and Worsnop, D. R.:
1071   Organic aerosol components observed in Northern Hemispheric datasets from aerosol mass
1072   spectrometry, Atmos. Chem. Phys., 10, 4625-4641, https://doi.org/10.5194/acp-10-4625-2010,
1073   2010.

1074 Onasch, T. B., Trimborn, A., Fortner, E. C., Jayne, J. T., Kok, G. L., Williams, L. R., Davidovits, P., and
1075   Worsnop, D. R. Soot particle aerosol mass spectrometer: Development, validation, and initial
1076   application. Aerosol Sci. Tech., 46, 804-817, http://dx.doi.org/10.1080/02786826.2012.663948,
1077   2012.

1078 Ou, Y., Nie, D., Chen, H., Ye, Z., Ge, X.: Characterization of products from the aqueous-phase
1079   photochemical oxidation of benzene-diols. Atmosphere, 12, 534,
1080   https://doi.org/10.3390/atmos12050534, 2021.

1081 Pan, Y., Ma, H., Li, Z., Du, Y., Liu, Y., Yang, J., and Li, G.: Selective conversion of lignin model veratryl
1082   alcohol by photosynthetic pigment via photo-generated reactive oxygen species, Chem. Eng. J.,
1083   393, 124772, https://doi.org/10.1016/j.cej.2020.124772, 2020.

1084 Raja, P., Bozzi, A., Mansilla, H., and Kiwi, J.: Evidence for superoxide-radical anion, singlet oxygen and
1085   OH-radical intervention during the degradation of the lignin model compound (3-methoxy-4-
1086   hydroxyphenylmethylcarbinol), J. Photochem. Photobiol. Chem., 169, 271-278,
1087   https://doi.org/10.1016/j.jphotochem.2004.07.009, 2005.

1088 Richards-Henderson, N. K., Hansel, A. K., Valsaraj, K. T., and Anastasio, C. Aqueous oxidation of green
1089   leaf volatiles by hydroxyl radical as a source of SOA: Kinetics and SOA yields, Atmos. Environ.,
1090   95, 105-112, http://dx.doi.org/10.1016/j.atmosenv.2014.06.026, 2014.

1091 Rossignol, S., Aregahegn, K. Z., Tinel, L., Fine, L., Nozière, B., and George, C.: Glyoxal induced
1092   atmospheric photosensitized chemistry leading to organic aerosol growth, Environ. Sci.
1093   Technol., 48, 3218-3227, https://doi.org/10.1021/es405581g, 2014.

1094 Scharko, N. K., Berke, A. E., and Raff, J. D.: Release of nitrous acid and nitrogen dioxide from nitrate
1095   photolysis in acidic aqueous solutions, Environ. Sci. Technol., 48, 11991-2001,
1096   https://doi.org/10.1021/es503088x, 2014.

1097 Simpson, C.D., Paulsen, M., Dills, R. L., Liu, L.-J.S., and Kalman, A.A. Determination of
1098   methoxyphenols in ambient atmospheric particulate matter: Tracers for wood combustion,
1099   Environ. Sci. Technol., 39, 631-637, https://doi.org/10.1021/es0486871, 2005.

1100   Smith, J. D., Kinney, H., and Anastasio, C.: Aqueous benzene-diols react with an organic triplet excited

1101   state and hydroxyl radical to form secondary organic aerosol. Phys. Chem. Chem. Phys., 17,

1102   10227, https://doi.10.1039/c4cp06095d, 2015.

1103   Smith, J. D., Kinney, H, and Anastasio, C.: Phenolic carbonyls undergo rapid aqueous photodegradation

1104   to form low-volatility, light-absorbing products, Atmos. Environ., 126, 36-44,

1105   https://doi.org/10.1016/j.atmosenv.2015.11.035, 2016.

1106   Smith, J. D., Sio, V., Yu, L., Zhang, Q., and Anastasio, C.: Secondary organic aerosol production from

1107   aqueous reactions of atmospheric phenols with an organic triplet excited state, Environ. Sci.

1108   Technol., 48, 1049-1057, https://doi.org/10.1021/es4045715, 2014.

1109   Stephen E. Stein (2014), NIST/EPA/NIH Mass Spectral Library with Search Program - SRD 1a, National

1110   Institute of Standards and Technology, https://doi.org/10.18434/T4H594 (Accessed 2022-04-29)

1111   Sun, Y., Zhang, Q., Anastasio, C., and Sun, J.: Insights into secondary organic aerosol formed via

1112   aqueous-phase reactions of phenolic compounds based on high resolution mass spectrometry,

1113   Atmos. Chem. Phys., 10, 4809–4822, https://doi.org/10.5194/acp-10-4809-2010, 2010.

1114   Tang, S., Li, F., Tsona, N.T., Lu, C., Wang, X., and Du, L.: Aqueous-phase photooxidation of vanillic

1115   acid: a potential source of humic-like substances (HULIS), ACS Earth Space Chem., 4, 862-

1116   872, https://doi.org/10.1021/acsearthspacechem.0c00070, 2020.

1117   Tsui, W. G., and McNeill, V. F. Modeling secondary organic aerosol production from photosensitized

1118   humic-like substances (HULIS), Environ. Sci. Technol. Lett., 5, 255-259.

1119   https://doi.org/10.1021/acs.estlett.8b00101, 2018.

1120   Verma, V., Fang, T., Xu, L., Peltier, R. E., Russell, A. G., Ng, N. L., and Weber, R. J.: Organic aerosols

1121   associated with the generation of reactive oxygen species (ROS) by water-soluble $PM_{2.5}$,

1122   Environ. Sci. Technol., 49, 4646-56, https://doi.org/10.1021/es505577w, 2015.

1123   Vione, D., Albinet, A., Barsotti, F., Mekic, M., Jiang, B., Minero, C., Brigante, M., and Gligorovski, S.:

1124   Formation of substances with humic-like fluorescence properties, upon photoinduced

1125   oligomerization of typical phenolic compounds emitted by biomass burning, Atmos. Environ.,

1126   206, 197-207, https://doi.org/10.1016/j.atmosenv.2019.03.005, 2019.

1127   Vione, D., Maurino, V., Minero, C., Pelizzetti, E., Harrison, M. A., Olariu, R. I., and Arsene, C.:

1128   Photochemical reactions in the tropospheric aqueous phase and on particulate matter, Chem.

1129   Soc. Rev., 35, 441-53, https://doi.org/10.1039/b510796m, 2006.

Vione, D., Maurino, V., and Minero, C.: Photosensitised humic-like substances (HULIS) formation processes of atmospheric significance: a review, Environ. Sci. Pollut. Res., 21, 11614-11622, https://doi.org/10.1007/s11356-013-2319-0, 2014.

Wang, J., and Wang, S. Reactive species in advanced oxidation processes: Formation, identification and reaction mechanism, Chem. Eng.J., 401, 126158, https://doi.org/10.1016/j.cej.2020.126158, 2020.

Wang, J., Ye, J., Zhang, Q., Zhao, J., Wu, Y., Li, J., Liu, D., Li, W., Zhang, Y., Wu, C., Xie, C., Qin, Y., Lei, Y., Huang, X., Guo, J., Liu, P., Fu, P., Li, Y., Lee, H. C., Choi, H., Zhang, J., Liao, H., Chen, M., Sun, Y., Ge, X., Martin, S. T., and Jacob, D .J.: Aqueous production of secondary organic aerosol from fossil-fuel emissions in winter Beijing haze. Proc. Natl. Acad. Sci. USA., 118, e2022179118, https://doi.org/10.1073/pnas.2022179118, 2021.

Wang, L., Lan, X., Peng, W., and Wang, Z.: Uncertainty and misinterpretation over identification, quantification and transformation of reactive species generated in catalytic oxidation processes: A review, J Hazard. Mater., 408, 124436, https://doi.org/10.1016/j.jhazmat.2020.124436, 2021.

Xu, X., Lu, X., Li, X., Liu, Y., Wang, X., Chen, H., Chen, J., Yang, X., Fu, T., Zhao, Q., and Fu, Q. ROS-generation potential of Humic-like substances (HULIS) in ambient $PM_{2.5}$ in urban Shanghai: Association with HULIS concentration and light absorbance, Chemosphere, 256, 127050, https://doi.org/10.1016/j.chemosphere.2020.127050 0045-6535, 2020.

Yang, J., Au, W. C., Law, H., Lam, C. H., and Nah, T.: Formation and evolution of brown carbon during aqueous-phase nitrate-mediated photooxidation of guaiacol and 5-nitroguaiacol, Atmos. Environ., 254, 118401, https://doi.org/10.1016/j.atmosenv.2021.118401, 2021.

Ye, Z., Zhuang, Y., Chen, Y., Zhao, Z., Ma, S., Huang, H., Chen, Y., and Ge, X.: Aqueous-phase oxidation of three phenolic compounds by hydroxyl radical: Insight into secondary organic aerosol formation yields, mechanisms, products and optical properties, Atmos. Environ., 223, 117240, https://doi.org/10.1016/j.atmosenv.2019.117240, 2020.

Yu, L., Smith, J., Laskin, A., Anastasio, C., Laskin, J., and Zhang, Q.: Chemical characterization of SOA formed from aqueous-phase reactions of phenols with the triplet excited state of carbonyl and hydroxyl radical, Atmos. Chem. Phys., 14, 13801–13816, https://doi.org/10.5194/acp-14-13801-2014, 2014.

Yu, L., Smith, J., Laskin, A., George, K. M., Anastasio, C., Laskin, J., Dillner, A. M., and Zhang, Q.:

Molecular transformations of phenolic SOA during photochemical aging in the aqueous phase: competition among oligomerization, functionalization, and fragmentation, Atmos. Chem. Phys., 16, 4511-4527, https://doi.org/10.5194/acp-16-4511-2016, 2016.

Zhang, T., Huang, S., Wang, D., Sun, J., Zhang, Q., Xu, H., Ho, S., Cao, J., and Shen, Z. Seasonal and diurnal variation of $PM_{2.5}$ HULIS over Xi'an in Northwest China: Optical properties, chemical functional group, and relationship with reactive oxygen species (ROS), Atmos. Environ., 268, 118782, https://doi.org/10.1016/j.atmosenv.2021.118782, 2022.

Zhang, X., Chen, Z. M., and Zhao, Y.: Laboratory simulation for the aqueous OH-oxidation of methyl vinyl ketone and methacrolein: significance to the in-cloud SOA production, Atmos. Chem. Phys., 10, 9551-9561, https://doi.org/10.5194/acp-10-9551-2010, 2010.

Zhao, R., Lee, A. K., and Abbatt, J. P.: Investigation of aqueous-phase photooxidation of glyoxal and methylglyoxal by aerosol chemical ionization mass spectrometry: observation of hydroxyhydroperoxide formation, J. Phys. Chem. A., 116, 6253-63, https://doi.org/10.1021/jp211528d, 2012.

Zhao, R., Mungall, E. L., Lee, A. K. Y., Aljawhary, D., and Abbatt, J. P. D.: Aqueous-phase photooxidation of levoglucosan-a mechanistic study using aerosol time of flight chemical ionization mass spectrometry (Aerosol ToF-CIMS), Atmos. Chem. Phys., 14, 9695-9706, https://doi.org/10.5194/acpd-14-8819-2014, 2014.

Zhao, R., Lee, A.K.Y., Huang, L., Li, X., Yang, F., and Abbat, J.P.D.Photochemical processing of aqueous atmospheric brown carbon, Atmos. Chem. Phys., 15, 6087-6100, https://doi.org/10.5194/acpd-15-2957-2015, 2015.

Zhou, Z., Chen, B., Qu, X., Fu, H., and Zhu, D.: Dissolved black carbon as an efficient sensitizer in the photochemical transformation of 17β-estradiol in aqueous solution, Environ. Sci. Technol., 52, 10391-10399, https://doi.org/10.1021/acs.est.8b01928, 2018.